







RESEARCH ARTICLE | APRIL 18 2024

## A zero-net-mass-flux wake stabilization method for blunt bodies via global linear instability

Qingchi Zhu (朱清驰) ; Lei Zhou (周蕾) ; Hongfu Zhang (张洪福) ; Kam Tim Tse (谢锦添) ; Hui Tang (唐辉) ; Bernd R. Noack 



*Physics of Fluids* 36, 043617 (2024)

<https://doi.org/10.1063/5.0202168>



View  
Online



Export  
Citation

### Articles You May Be Interested In

Aero-thermal numerical characterization of blunt fin-induced shock wave–boundary layer interaction and its control through leading-edge cooling injection

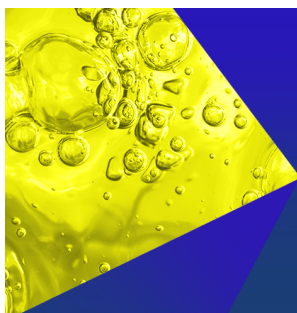
*Physics of Fluids* (September 2022)

Stability analysis of streamwise vortices over a blunt inclined cone under a hypersonic flight condition

*Physics of Fluids* (July 2022)

Drag reduction of a blunt body through reconfiguration of rear flexible plates

*Physics of Fluids* (April 2021)



**Physics of Fluids**  
Special Topics  
Open for Submissions

[Learn More](#)

# A zero-net-mass-flux wake stabilization method for blunt bodies via global linear instability

Cite as: Phys. Fluids **36**, 043617 (2024); doi: [10.1063/5.0202168](https://doi.org/10.1063/5.0202168)

Submitted: 2 February 2024 · Accepted: 21 March 2024 ·

Published Online: 18 April 2024



View Online



Export Citation



CrossMark

Qingchi Zhu (朱清驰),<sup>1</sup> Lei Zhou (周蕾),<sup>2,a)</sup> Hongfu Zhang (张洪福),<sup>1,a)</sup> Kam Tim Tse (谢锦添),<sup>2</sup> Hui Tang (唐辉),<sup>3</sup> and Bernd R. Noack<sup>4,5</sup>

## AFFILIATIONS

<sup>1</sup>School of Civil Engineering and Transportation, Northeast Forestry University, Harbin 150040, China

<sup>2</sup>Department of Civil and Environmental Engineering, The Hong Kong University of Science and Technology, Clear Water Bay, Kowloon, Hong Kong, China

<sup>3</sup>Department of Mechanical Engineering, The Hong Kong Polytechnic University, Hong Kong, China

<sup>4</sup>Chair of Artificial Intelligence and Aerodynamics, School of Mechanical Engineering and Automation, Harbin Institute of Technology, Shenzhen 518055, China

<sup>5</sup>Guangdong Provincial Key Laboratory of Intelligent Morphing Mechanisms and Adaptive Robotics, Harbin Institute of Technology, Shenzhen 518055, China

<sup>a)</sup>Authors to whom correspondence should be addressed: [lzhouau@connect.ust.hk](mailto:lzhouau@connect.ust.hk) and [zhanghongfu@nefu.edu.cn](mailto:zhanghongfu@nefu.edu.cn)

## ABSTRACT

A rectangular cylinder, with an aspect ratio of 5, is a widely used bluff body in engineering practice. It undergoes intricate dynamical behavior in response to minute alterations in the flow angle of attack ( $\alpha$ ). These modifications invariably precipitate the failure of wake control for classical flow control methods with various  $\alpha$  values. In this study, global linear instability, adjoint method, and sensitivity analysis are employed to identify the optimal position for flow control. It is found that the sensitive region gradually transitions from the leeward side to the downwind side of the model as  $\alpha$  and Reynolds number ( $Re$ ) increase. So, we set up airflow orifices for flow control in both positions. Jet flow control on the leeward side effectively inhibits vortex shedding ( $\alpha \leq 2^\circ$ ). High-order dynamic mode decomposition is employed to reveal the inherent mechanism of control. Suction control on the downside effectively mitigates the shear layer separation phenomenon induced by the altered spatial structure associated with higher  $\alpha$ . A novel zero-net-mass-flux wake control, bionics-based breathe-valve control (BVC), is proposed to optimize the control effect. BVC is applicable for various  $\alpha$  and  $Re$ , with optimal effectiveness achievable through jet velocity adjustments. The prediction-control approach in this investigation provides a targeted method to mitigate flow-induced vibration.

Published under an exclusive license by AIP Publishing. <https://doi.org/10.1063/5.0202168>

## I. INTRODUCTION

As a classical structural configuration, the blunt body has garnered considerable attention in civil and marine engineering, such as high-rise buildings, long-span bridges, and offshore platforms.<sup>1,2</sup> As the fluid flows past the blunt body, its significant drag effect causes asymmetric periodic vortex shedding. Alternating vortex shedding not only reduces the stability of the near wake, but generates unsteady forces on the blunt body. This phenomenon contributes to flow-excited vibration problems.<sup>3–8</sup> Flow-induced vibrations tend to change the flow structure around the blunt body, which can lead to potential structural fatigue and engineering accidents.<sup>9</sup> Controlling vortex shedding is a crucial method for mitigating flow-induced vibrations.

Flow control methods are typically categorized into two types: passive flow control and active flow control.<sup>10</sup> Passive flow control

requires no external energy input and usually only requires changing the shape of the object or installing additional facilities to change flow structure, such as surface protrusions, grooves, and splitter plates control rods.<sup>11–14</sup> Nevertheless, the simple passive control method exhibits a limited capacity to regulate and adapt to intricate changes and other challenges. Active flow control (AFC) has been proposed to change the flow development path to a more desirable state.<sup>15</sup> AFC can harness the intrinsic characteristics of the flow based on the specific external conditions of the object, employing minor localized power inputs for flexible control adjustments.<sup>16</sup> Also, AFC with energy input can significantly improve aerodynamic stability. The classical forms of blunt bodies are usually cylinders, square cylinders, etc., and their AFCs are also widely studied. Among these methods, suction and blowing represent the most widely employed techniques in active flow control.<sup>17</sup>

Delaunay and Kaiktsis investigated the effect of base suction and blowing on the stability and dynamics of a cylindrical wake at low Reynolds number conditions ( $Re \leq 90$ ) by numerical simulation and stability analysis. It is found that a slight blowing can stabilize the wake when  $Re > 47$  and a high enough suction momentum can reduce the absolute instability of the near wake.<sup>18</sup> Fransson *et al.* conducted an analysis on vortex shedding frequency, and wake flow behind a porous circular cylinder under the influence of continuous suction or blowing through the cylinder walls. The findings reveal that even modest levels of suction/blowing exert a significant influence on the flow around the cylinder.<sup>19</sup> Chen *et al.* employed the suction flow method to manage the vortex-induced vibration of a cylinder. The study reveals the effectiveness of suction flow control in dampening vortex-induced vibrations, particularly when the suction flow velocity is below the head-on flow velocity.<sup>20</sup> Gao *et al.* conducted an experimental investigation to explore the effectiveness and mechanism of a bluff-body control concept characterized by combined windward suction and leeward blowing (WSLB). Experimental findings illustrate that the application of WSLB control reduces sectional drag at the midspan and diminishes the fluctuating amplitudes of dynamic wind loads acting on the cylinder.<sup>21</sup> Fan *et al.* applied deep reinforcement learning to investigate the most effective active control method in the flow around a cylinder.<sup>22</sup> Square cylinders deserve attention due to their pronounced blunt body characteristics.<sup>23–26</sup> Gao *et al.* effectively suppressed the instability of vortex shedding in the wake through experiments using the jet method at the stagnation points before and after the square cylinder.<sup>27</sup> Ran *et al.* further verified by means of numerical simulation that the windward control can effectively reduce the drag coefficient of the square column, while the leeward control significantly suppresses the fluctuating lift coefficients.<sup>28</sup> Extending the square cylinder to practical engineering, Zhang *et al.* arranged three parallel rows of suction holes along the bridge spreading direction to trigger or amplify mode A destabilization to suppress the trailing-edge vortices, and then suppress the vortex-induced vibration.<sup>29</sup> Chen *et al.* designed leading-edge suction and trailing-edge jet (LSTJ) to control the unsteady flow structure around the bridge. Through surface pressure and particle image velocimetry (PIV) measurements, it was observed that LSTJ diminished the intensity of wake vortices and efficiently mitigated the effects of vortex-induced vibrations.<sup>30</sup>

In the field of mechanical engineering, the blunt body problem is specifically found in aircraft wings, gas pipes, radiator panels, etc.<sup>31–35</sup> The practical components of the project will assume varying sizes based on their intended functions, simplifying to rectangles with distinct aspect ratios. The aerodynamic characteristics of the simplified rectangular structure can be categorized into three states according to its aspect ratio: separated state, intermittent reattachment state, and complete reattachment state.<sup>36,37</sup> The Rectangular Cylindrical Aerodynamic Benchmark (BARC) was introduced during the sixth International Colloquium on Bluff Body Aerodynamics and Applications in 2008.<sup>38</sup> Its purpose was to examine the flow characteristics of the short side of a rectangular cylinder with an aspect ratio of 5 ( $Ar = 5$ ).<sup>39–41</sup> Based on this criterion, numerous wind-tunnel and water-tunnel experiments<sup>42</sup> have been carried out on rectangular cylinders with  $Ar = 5$  to investigate the associated flow structure and vortex dynamics.<sup>43,44</sup> The majority of the aforementioned investigations concentrate on turbulent flows, specifically at higher Reynolds numbers, with a limited number of studies conducted at low Reynolds

numbers.<sup>45</sup> In laminar flows at low Reynolds numbers, the complications arising from high Reynolds numbers, such as Carman's vortex shedding influence, can be excluded. This allows for an intuitive analysis of the dominant factors in flow phenomena.<sup>46–50</sup> Simultaneously, fluids frequently alter the direction of their flow in response to environmental influences.<sup>51</sup> Most current research has concentrated on higher angles of attack, which are more prone to induce flow separation.<sup>52,53</sup> Examining smaller angle of attack contributes to comprehending the behavior and interaction of fluids within the boundary layer, enhancing the theoretical understanding of hydrodynamic phenomena.<sup>54</sup>

Hence, the objective of this investigation is to mitigate the potential impact of vortex shedding on the flow structure of a rectangular cylinder with  $Ar = 5$  at low Reynolds numbers under various angles of attack through the application of active control. However, most of the active flow control methods in the current research are energy-consuming and complex, and are mostly suggested by trial-and-error methods through experiments and numerical simulations.<sup>55</sup> Sensitive analysis-based control offers a theoretical framework for predicting the optimal location for placing control elements to mitigate global instability, facilitating the design of effective controls. Global linear instability and receptivity analysis using the adjoint method are performed. The sensitivity map to localized feedback is subsequently acquired, providing information on the optimal location for placing the jet flow.<sup>56–60</sup> In this study, based on the application of sensitivity analysis, active flow control measures are laid out in a targeted manner, and conclusions on control measures with generalizability are summarized. Simultaneously, higher-order dynamic mode decomposition (HODMD) is employed to scrutinize the nuanced alterations in the flow structure during the establishment of the control solution.<sup>61</sup> HODMD facilitates the categorization of modes based on their dynamic activity, identifies predominant modes, and has the capability to mitigate specific perturbative factors.<sup>62–65</sup> The implementation of active flow control often focuses solely on the control effect while neglecting the flow input considerations.<sup>28,66,67</sup> Additional mass source inputs are frequently required for wind-tunnel experiments and practical engineering.<sup>19,20,68,69</sup> It increases the cost and complexity of both scientific research and engineering applications. In this study, the concept of bionics-based respiratory motion is introduced, and the breathe-valve control (BVC) method is proposed to ensure unobstructed flow. BVC is a combination of suction and jet, which ensures the control effect without adding additional mass sources and exhaust means. BVC effectively simplifies system design and reduces energy costs.

In this article, Sec. II provides the details of simulation methods, computational strategies, and sensitive analysis methods; Sec. III introduces the validation of simulation methodology; Sec. IV introduces linear stability and sensitivity analysis and compares the control effect of normal AFC and BVC. The simulation exclusively contemplates the incoming flow from the left side and a positive angle of attack. Consequently, the analysis performed is limited to the present scope. The research process of this paper has been summarized in a graphical abstract as shown in Fig. 1.

## II. NUMERICAL METHODOLOGY AND SURROGATE MODEL

This section commences with an introduction to the linear stability and sensitivity analysis methods employed to identify the optimal

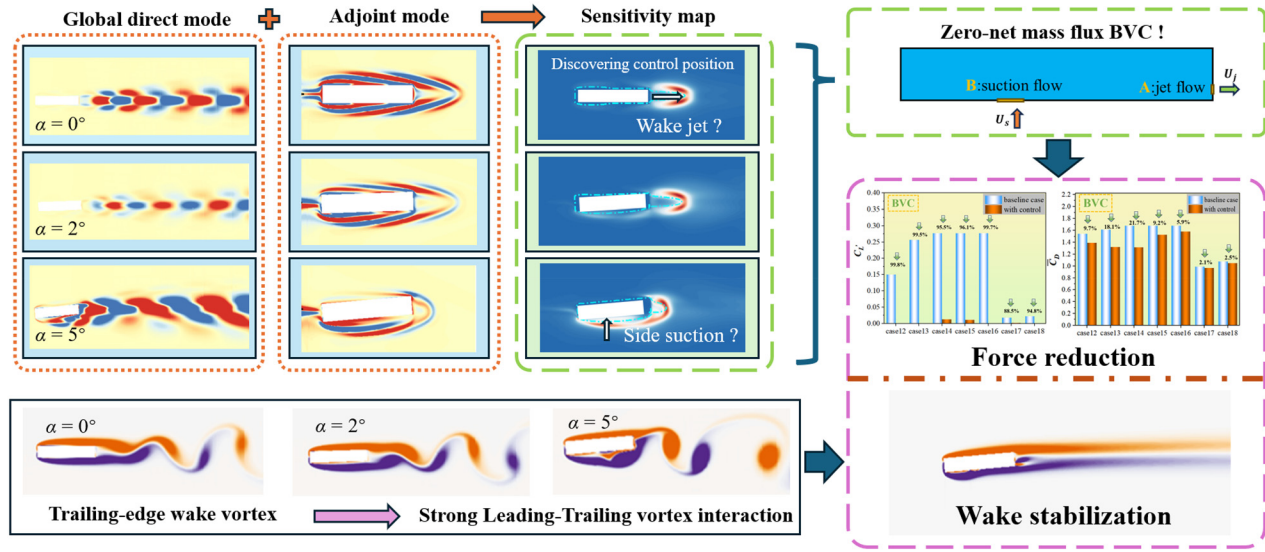


FIG. 1. Graphical summary of the research process.

location to control the flow. Then, the details of the simulation methodology and computational strategy of this study are shown.

### A. Linear stability and sensitive analysis method

To improve the sensitivity to local momentum-forcing feedback, acquiring both direct and concomitant modes is a prerequisite. The flow stability and instability of rectangular cylinders ( $AR=5$ ) are examined through linear stability analysis.

Initially, the instantaneous flow  $(u, p)$  can be decomposed into the sum of baseflow  $(U_b, P_b)$  and infinitesimal perturbations  $(\hat{u}, \hat{p})$ . Then, the incompressible Navier–Stokes equations can be linearized. In this context, the base flow is selected as the time-averaged or steady-state flow computed through the nonlinear Navier–Stokes equations. In the linear stability analysis, perturbations can be expressed in the form of normal modes  $(\hat{u}(x, y, t), \hat{p}(x, y, t))^T = (\hat{u}(x, y), \hat{p}(x, y))^T \exp(\sigma t)$  with  $\sigma = \lambda + i\omega$ , where the real part  $\lambda$  and the imaginary part  $\omega$  are the growth rate and frequency of the mode, respectively. The Navier–Stokes equations linearized around the base flow  $(U_b, P_b)$  can then be written as

$$\sigma \hat{u} + \nabla \hat{u} \cdot U_b + \nabla U_b \cdot \hat{u} = -\nabla \hat{p} + \frac{1}{Re} \nabla^2 \hat{u}, \quad \nabla \cdot \hat{u} = 0. \quad (1)$$

The boundary conditions for Eq. (1) align with those found in the nonlinear Navier–Stokes equations, differing only in the inlet boundary condition involving  $\hat{u} = 0$ .

The adjoint method serves as a powerful tool in the realms of flow control and form optimization. The adjoint equation of the linearized Navier–Stokes equations can be expressed as

$$\sigma^* \hat{u}^+ - \nabla \hat{u}^+ \cdot U_b + (\nabla U_b)^T \cdot \hat{u}^+ = -\nabla \hat{p}^+ + \frac{1}{Re} \nabla^2 \hat{u}^+, \quad (2)$$

$$\nabla \cdot \hat{u}^+ = 0,$$

where  $\hat{u}^+$  and  $\hat{p}^+$  are the adjoint vectors to  $\hat{u}$  and  $\hat{p}$ , respectively. The boundary conditions for Eq. (2) are  $\hat{u}^+ = 0$  at the inlet and walls,

$\hat{p}^+ n - Re^{-1}(\nabla \hat{u}^+) \cdot n = (U_b \cdot n) \hat{u}^+$  at the outlet. However, the spectral element method is difficult to apply to such boundary conditions. Instead, identical boundary conditions as those at the inlet  $\hat{u}^+ = 0$  are employed. It is rational as the adjoint mode rapidly decays away from the bluff bodies.

Regarding sensitivity to local feedback, Giannetti and Luchini<sup>57</sup> introduced the concept of the “wavemaker” to denote regions where generic structural alterations in the stability problem cause the most significant shift in the leading eigenvalue. To identify the wavemaker region, they examined variations in the leading eigenvalue arising from spatially localized feedback in the momentum equations. Assuming the feedback process is concentrated at the station  $(x_0, y_0)$ . The introduction of a force, denoted as  $f(x, y)$ , into Eq. (2) and proportionate to the global mode velocity, can be expressed by

$$\hat{f} = C_0 \delta(x - x_0, y - y_0) \hat{u}, \quad (3)$$

where  $C_0$  is a matrix operator and  $\delta(x - x_0, y - y_0)$  is the Kronecker symbol. The variations  $\delta\sigma$  can be expressed by

$$|\delta\sigma(x_0, y_0)| \leq \|C_0\| \cdot \|\hat{u}(x_0, y_0)\| \cdot \|\hat{u}^+(x_0, y_0)\|. \quad (4)$$

Observe that the adjoint global mode requires normalization with  $\langle \hat{u}, \hat{u}^+ \rangle = 1$ . In Eq. (4), the principal eigenvalue is responsive to local feedback solely within the overlapping domain of the direct and adjoint global modes. Hence, Eq. (4) serves to identify locations with stronger feedback, delineating regions where the instability mechanism operates.

### B. Direct numerical simulation (DNS)

Simulating the flow dynamics surrounding a rectangular cylinder with ( $Ar=5$ ) entails solving the time-dependent two-dimensional Navier–Stokes equations within a Cartesian reference frame. The flow is considered incompressible, Newtonian, laminar, and unstable. As a



result, the governing equations for the flow dynamics in this configuration are expressed as follows:

$$\frac{\partial u}{\partial t} = -(u \cdot \nabla)u - \nabla p + \frac{1}{Re} \nabla^2 u, \quad (5)$$

$$\nabla \cdot u = 0. \quad (6)$$

In the equation,  $p$  represents the pressure, and  $u$  represents the instantaneous velocity vector. To maintain dimensionlessness, the physical quantities are normalized by inlet velocity ( $U$ ) and rectangular cylinder width ( $D$ ) of the system.

Figure 2(a) illustrates the boundary conditions, layout position, and fixation of the computational model. The length of the rectangular cylinder ( $AR=5$ ) is set to  $B$ , the width is set to  $D$ , and  $AR=B/D=5$ . The length of the computational domain in the  $x$ -axis direction is  $15B=75D$ , and the velocity inlet is  $25D$  from the midpoint of the model; The length of the computational domain in the  $y$ -axis direction is  $40D$ , with symmetric boundary conditions on the upper and lower sides, with a distance of  $20D$  from the midpoint of the model. The rectangular cylinder model is set to wall for fixed form. The variation in the flow angle of attack ( $\alpha$ ) is simulated by adjusting the angle between the model's horizontal axis and the  $x$  axis. The overall mesh is constructed using the open source software "Gmsh" and is set up as a

structured mesh.<sup>70</sup> As shown in Fig. 2(b), the boundary layers of the model are meshed with a resolution of  $0.01D$  along the  $x$  and  $y$  directions, and the length of the mesh elements is uniformly distributed around the model. The mesh stretch ratio in the wall boundary layer is set to equal 1.05, and 25 layers are encrypted. The resolution is coarse to a maximum of  $0.04D$  away from the boundary layer, maximum  $\Delta x/B=0.006$  and maximum  $\Delta y/B=0.001$ . The Navier–Stokes equation is solved by the finite volume method using the implicit pressure solver in ANSYS Fluent 19.2. In this context, the convective term is discretized using the second-order upwind scheme, while the time-ahead term is treated with the implicit bounded second-order scheme. At the entrance to the calculation domain, a Dirichlet boundary condition ( $u=U$ ,  $v=0$ ) is imposed, and at the outlet, the pressure outlet condition with zero static gauge pressure is imposed. The variables  $u$  and  $v$  denote the velocity components in the  $x$  and  $y$  directions, respectively, and  $U$  represents the inflow flow rate, which is set to 1 m/s. Symmetric boundary conditions were applied to the upper and lower sides, and no-slip wall boundary conditions ( $u=0$ ,  $v=0$ ) were adopted on the surface of twin cylinders. The settings related to BVC will be explained at Sec. IV.

### III. GRID SENSIBILITY ANALYSIS

The results of the comparisons in this section are summarized in Table I. To ensure the precision of the numerical simulations, varying mesh densities are employed in this section to verify mesh independence. Grid volumes of 29 306, 48 708, and 79 786 are employed for comparison. To conserve computational resources while maintaining numerical simulation accuracy, a configuration with a grid volume of 48708 is employed. The results are also compared with other experimental results and numerical simulations on rectangular cylinders ( $AR=5$ ). The drag coefficient  $C_D$ , the lift coefficient  $C_L$ , and the Strouhal number  $St$  are defined as follows:

$$C_D = \frac{F_D}{0.5\rho U^2 D}, \quad (7)$$

$$C_L = \frac{F_L}{0.5\rho U^2 D}, \quad (8)$$

$C_L'$  is the fluctuation value of  $C_L$ ,

$$St = fD/U, \quad (9)$$

where  $F_D$  and  $F_L$  are the measured drag and lift forces, respectively;  $\rho$  is the fluid density;  $U$  is the free-stream velocity. The outcomes of

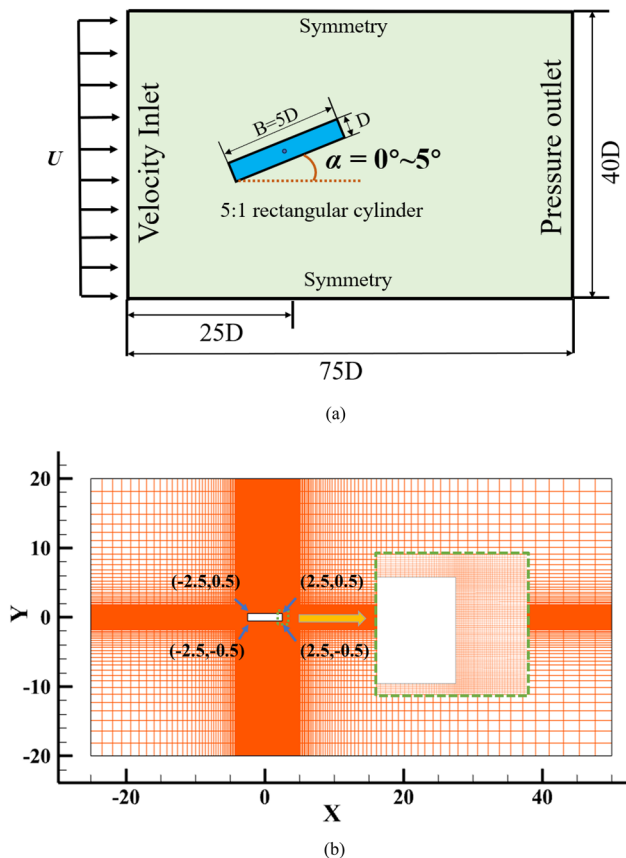


FIG. 2. (a) The schematic diagram of computational domain and boundary conditions. (b) Computational domain and mesh.

TABLE I. Tests of independence of rectangular cylinder meshes ( $AR=5$ ) and comparison with earlier literature.

	Grid	$Re$	$St$	$C_D$
Present stationary case ( $\alpha=0^\circ$ )	29 306	150	0.1105	1.023 3
	48 708		0.1199	1.090 8
	76 786		0.1232	1.097 6
Hourigan <i>et al.</i> <sup>71</sup>	...	400	...	1.089 0
Nakamura <i>et al.</i> <sup>72</sup>	...	5500–55 000	~0.1150	...
Schewe <i>et al.</i> <sup>44</sup> (Experiments)		20 000	0.1110	1.029
Zhu <i>et al.</i>	82 792	400	0.1020	1.012

crucial parameters,  $St$  and  $C_D$ , demonstrated a strong correspondence, thereby reinforcing the accuracy and feasibility of this investigation.

#### IV. RESULTS AND DISCUSSION

##### A. Summary and selection of baseline cases

In this section, the root mean square of  $C_L$  ( $C_{L-RMS}$ ) and power spectral density (PSD) peak values are first analyzed. For the bluff bodies,  $C'_L$  is always served as an indicator of wake fluctuation. Thus, the evaluation of the control effectiveness hinges on scrutinizing alterations in the  $C'_L$  magnitude. The variation of the mean drag coefficient ( $\bar{C}_D$ ) is also presented to demonstrate the optimization of the hydrodynamic effect. Thus, in this section,  $C'_L$  and  $\bar{C}_D$  are presented here. As shown in Fig. 3(a), the  $C_{L-RMS}$  at all  $Re$  shows an increasing trend as the  $\alpha$  increases. It is also noticeable that the higher the  $Re$  ( $Re = \frac{UL}{\nu}$  where  $U$  is the incoming flow velocity,  $\nu$  is the coefficient of kinematic viscosity, and  $L$  is the height of the surface facing the flow), the greater the amplitude of the elevation. The effect of  $Re$  on  $C_{L-RMS}$  is observed, and it is found that an increase in  $Re$  is accompanied by an increase in  $C_{L-RMS}$ . Meanwhile, the larger the  $\alpha$ , the more significant the effect of  $Re$ , i.e., the growth gradient of  $C_{L-RMS}$  increases accordingly. The increasing  $C_{L-RMS}$  implies an enhanced interaction of the flow field with the model. As shown in Fig. 3(b), the PSD peak value corresponding to the primary vortex shedding frequency for each case has the same trend as the  $C_{L-RMS}$ . The pinnacle in the PSD typically indicates the magnitude of vortex energy. A rise in this peak value denotes a heightened complexity in the flow structure, accompanied by a more pronounced and intensified vortex shedding phenomenon. Figure 3(c) also directly confirms this point. The low angle-of-attack cases have no strong vortex shedding at low  $Re$  due to the stable space structure. This responds as a sudden decrease in  $St$ , but fades as the flow angle of attack increases. Flow structures characterized by elevated energy value are frequently associated with potential loading effects. These effects, in turn, may indirectly instigate flow-induced vibrations, thereby augmenting the risk of engineering accidents. Therefore, from the consideration of two sensitive parameters for  $\alpha$  and  $Re$ , representative cases are selected to be analyzed. The vortices for the selected cases are shown in Fig. 4 as the baseline case for the analysis. Illustrated in Figs. 4(a), 4(b), and 4(d), while maintaining a constant  $Re$ , an elevation in the  $\alpha$  induces premature separation of the shear layer on the model's lower side. This phenomenon changes the flow structure near the model and accelerates the generation of vortex shedding, that is,  $St$  improves. Similarly, the same effect is observed when the  $\alpha$  is maintained constant as shown in Figs. 4(c), 4(d), and 4(e). The alternating impacts of the shear layer on the trailing edge of the model resulted in vortex shedding, which reflects the instability of the shear layer. The vortex shedding pattern shows a 2S pattern.

##### B. Linear stability and sensitivity analysis

Linear stability and sensitivity analyses were conducted to identify the wavemaker regions associated with the rectangular cylinder. Identified wavemaker regions have the potential to serve as optimal locations for implementing flow control. The baseline case was defined using the time-averaged flow state. Significantly, the time-averaged flow field demonstrates superior predictive capability for the vortex shedding frequency compared to the steady flow field obtained through the selective frequency damping method. However, our

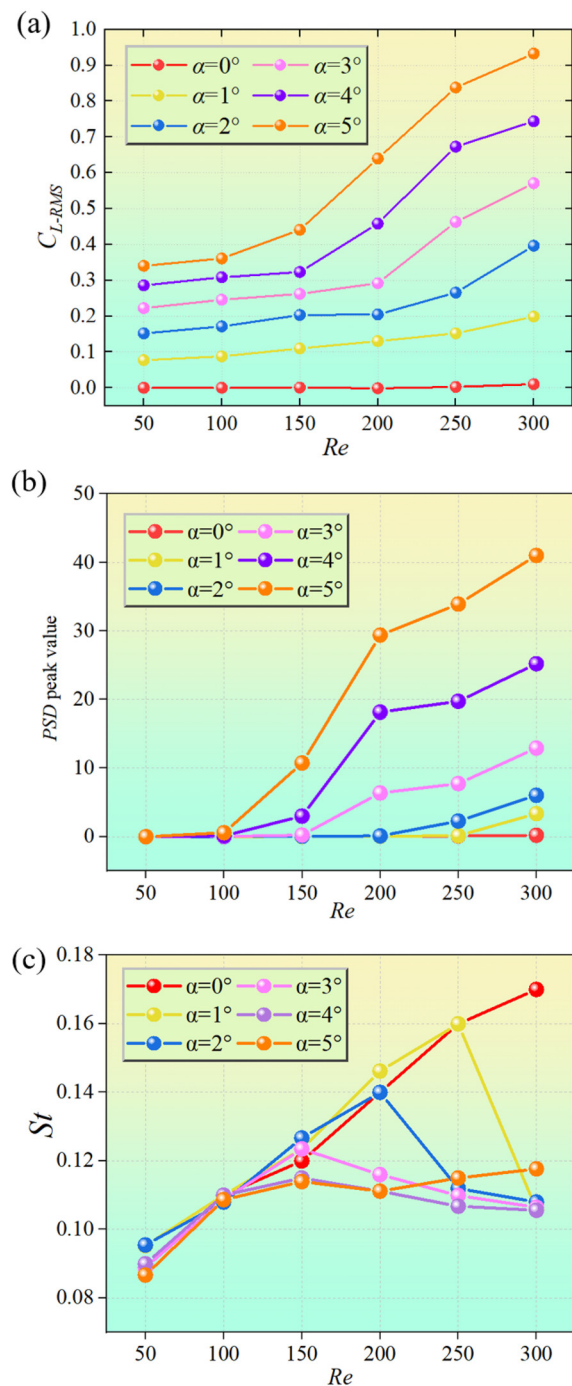
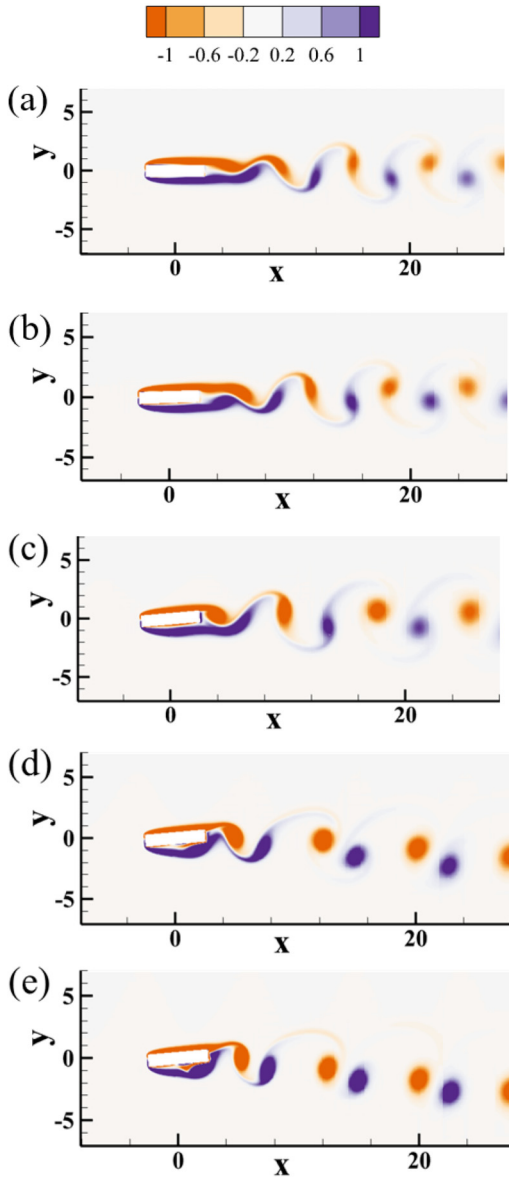


FIG. 3. (a)  $C_{L-RMS}$ , (b) PSD peaks value, and (c)  $St$  for rectangular cylinder ( $AR = 5$ ) at various  $\alpha$  and  $Re$ .

emphasis remains solely on the identification of the wavemaker region, a task achievable through the analysis of direct/adjoint modes.

Figures 5 and 6 illustrate the leading direct/adjoint global mode for each baseline case of Fig. 4, respectively. For the leading direct



**FIG. 4.** Vorticity of the baseline case at (a)  $\alpha = 0^\circ$ ,  $Re = 200$ , (b)  $\alpha = 2^\circ$ ,  $Re = 200$ , (c)  $\alpha = 5^\circ$ ,  $Re = 150$ , (d)  $\alpha = 5^\circ$ ,  $Re = 200$ , and (e)  $\alpha = 5^\circ$ ,  $Re = 250$ .

global mode, the modes show symmetric characteristics when  $\alpha = 0^\circ$ . The real part of the modes bears resemblance to the imaginary counterpart, featuring a certain phase shift (not depicted here). The leading direct global mode is only observed in the wake region at the trailing edge of the model when  $\alpha = 0^\circ$ . As depicted in Figs. 5(a), 5(b), and 5(d), the modes exhibit a tilt as  $\alpha$  increases. The modal boundaries between the upper and lower sides become progressively indistinct, and the modes of the upper side and the middle part gradually amalgamate. This process is accelerated by the increase in  $Re$ . Illustrated in Figs. 5(c), 5(d), and 5(e), the modes within the wake region have completely amalgamated, signifying the initiation of the separation

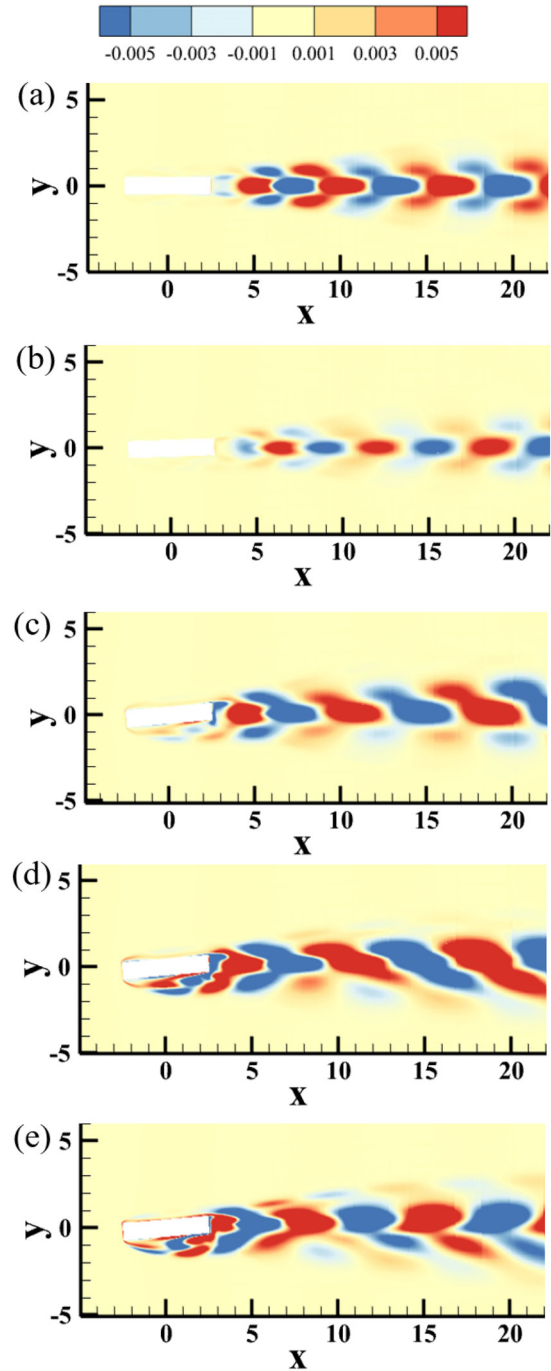


**FIG. 5.** The leading direct global mode at (a)  $\alpha = 0^\circ$ ,  $Re = 200$ , (b)  $\alpha = 2^\circ$ ,  $Re = 200$ , (c)  $\alpha = 5^\circ$ ,  $Re = 150$ , (d)  $\alpha = 5^\circ$ ,  $Re = 200$ , and (e)  $\alpha = 5^\circ$ ,  $Re = 250$ .

state for the subsequent cycle. Moreover, the increase in  $\alpha$  and  $Re$  drives the leading direct global mode on the lower side of the model to become more pronounced and complex. This implies that global instability is primarily governed by leeward regional flow and downside flow.

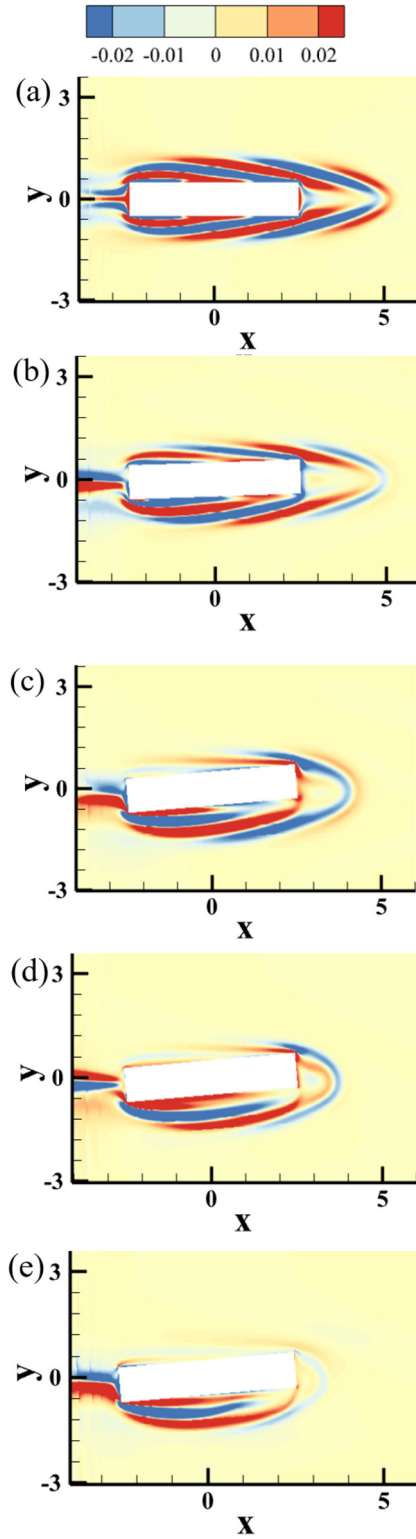


**FIG. 6.** The adjoint mode at (a)  $\alpha = 0^\circ$ ,  $Re = 200$ , (b)  $\alpha = 2^\circ$ ,  $Re = 200$ , (c)  $\alpha = 5^\circ$ ,  $Re = 150$ , (d)  $\alpha = 5^\circ$ ,  $Re = 200$ , and (e)  $\alpha = 5^\circ$ ,  $Re = 250$ .

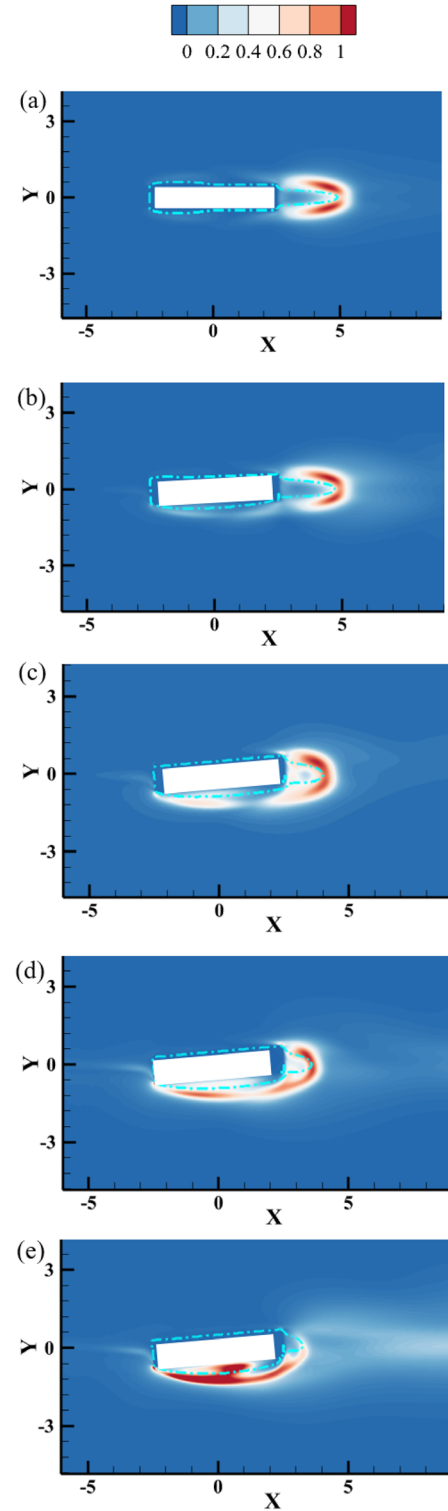


**FIG. 7.** Sensitivity map to a local feedback at (a)  $\alpha = 0^\circ$ ,  $Re = 200$ , (b)  $\alpha = 2^\circ$ ,  $Re = 200$ , (c)  $\alpha = 5^\circ$ ,  $Re = 150$ , (d)  $\alpha = 5^\circ$ ,  $Re = 200$ , and (e)  $\alpha = 5^\circ$ ,  $Re = 250$ . The blue dot lines are the dividing streamline delimiting the recirculation flow.



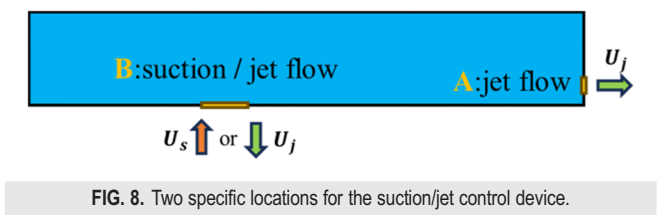


FIG. 8. Two specific locations for the suction/jet control device.

Regarding the adjoint modes, they serve as a direct reflection of the receptivity of flow structures to momentum forcing. Similar to the direct instability modes, the adjoint modes of the downstream velocity at  $\alpha = 0^\circ$  exhibit symmetric modes. Here, the adjoint modes are evident all around the model, indicating that the model is surrounded by regions that will affect the flow structure. Alike the leading direct global mode, the raising of  $\alpha$  and  $Re$  in Fig. 6 gradually concentrates the adjoint modes below the leeward side of the model as well as on the downside.

Figure 7 outlines the sensitivity map (directly reflecting the wave-maker region) to local feedback for each baseline case of Fig. 4, respectively. Structural sensitivity discloses the spatial region most responsive to flow perturbation. Like the adjoint modes, the elevation of  $\alpha$  causes the otherwise symmetrical sensitive region at the leeward side to gradually evolve to concentrate toward the lower right. At high  $\alpha$ , the increase in  $Re$  makes the sensitive region below the model more pronounced, tending to the lower left side. The above linear stability and sensitivity analysis offer the direction and foundation for subsequent flow control strategies.

C. Active flow control

In this section, the effect of active flow control on rectangular cylinders ( $AR = 5$ ) is systematically investigated. The fluctuation of the lift coefficient ( $C_L$ ) is usually directly related to the instability and turbulence of the flow. We established two active control zones, informed by the sensitivity regions delineated in the summary provided in Fig. 7 for each baseline case. As shown in Fig. 8, following the definition of Zhou *et al.*<sup>60</sup> the jet momentum coefficient is defined as  $C_q = U_{jet}d/UD = 0.1U_j$ . The lower side of the sensitivity map has a larger range when the flow angle of attack is higher. To enlarge the control area, set airflow orifice B to twice the size of A. The airflow orifice A of length  $L_1 = l_1/D = 0.1$  is set below the leeward side of the model, and the upper part of the orifice is located at the distance of  $D_1 = d_1/D = 0.25$  from the midpoint. The airflow orifice B of length  $L_2 = l_2/D = 0.2$  is set on the left side of the lower side of the model, and the right side of the orifice is located at the distance of  $D_2 = d_2/D = 0.5$  from the midpoint.

TABLE II. Parameters for each case of flow control via airflow orifice A.

Case	Flow angle of attack ( $\alpha$ ) (deg)	Re	Airflow orifice A	
			Flow control	$U_j$
Case 1	0	200	Jet	1
Case 2	2	200		
Case 3	5	150		
Case 4	5	200		
Case 5	5	250		

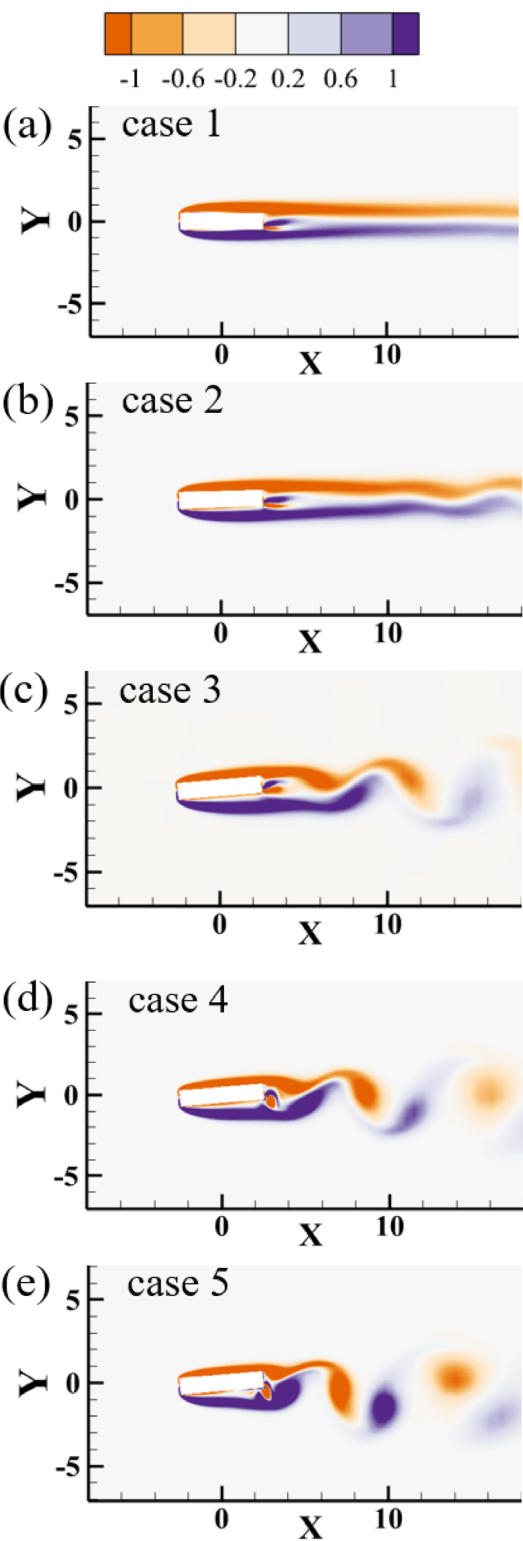


FIG. 9. Vorticity for each case after flow control by airflow orifice A: (a) case 1, (b) case 2, (c) case 3, (d) case 4, and (e) case 5.

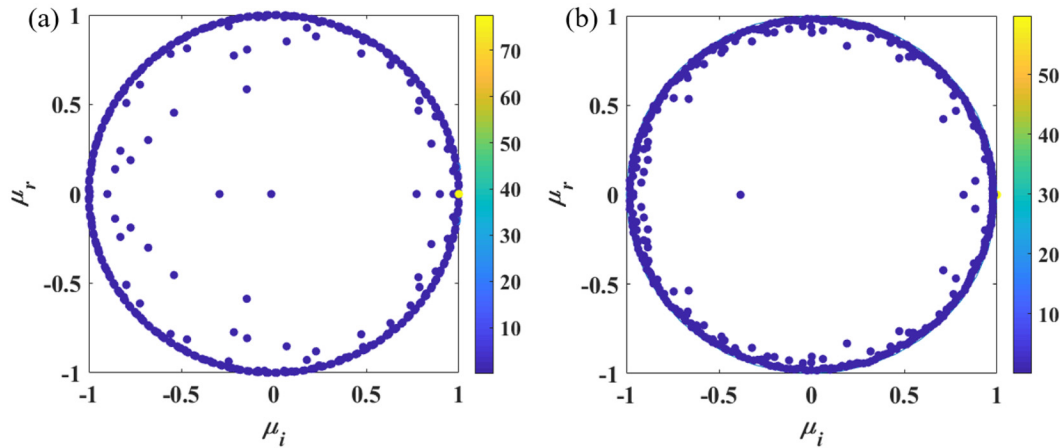


FIG. 10. Ritz eigenvalues for (a) baseline case and (b) case 1.

The suction flow velocity is  $U_s = u_s/U$ , and the jet flow velocity is  $U_j = u_j/U$ , where  $d_1$ ,  $d_2$ ,  $l_1$ , and  $l_2$  are the actual lengths, as well as  $u_s$  and  $u_j$  are the actual velocities. The above definitions are dimensionless. The control method uses the common suction and jet method, airflow orifice A and B form the BVC. The specific application of which is described in detail later.

### 1. Airflow orifice A jet and HODMD

In this section, flow control is accomplished by adjusting airflow orifice A. As depicted in Fig. 7, the leeward facet of the model consistently emerges as a region sensitive to flow structure changes. Jets are employed to retard the separation of the shear layer. This measure can influence the formation of vortex core and the evolution of vortices in the flow field, which can contribute to delaying or inhibiting vortex shedding. Specific control measures for each case are listed as shown in Table II.

Figure 9 shows the vortices after control for each case. In comparison with Fig. 3(a), after the implementation of flow control (case 1),

the flow structures on the upper and lower sides no longer interfere with each other, and vortex shedding in the wake is absent. The phenomenon is the same as the laminar flow phenomenon at extremely low Reynolds number. This suggests that the jet is effectively regulated to suppress the ongoing separation of the shear layer and maintain the stability of the flow field structure consistently. The situation in case 2 is consistent with case 1, with only slight fluctuations in the wake. This implies that rectangular cylinders ( $AR = 5$ ) at low flow angle of attack can be constrained by implementing jets at the leeward end to inhibit vortex shedding.

To elucidate the restraining impact of the jet from a mechanistic perspective, higher-order dynamic mode decomposition (HODMD) is employed to contrast the baseline scenario of case 1 with the jet flow control. The data were collected after the full development of the flow. The dataset comprises 40 oscillation cycles, with each cycle consisting of 25 samples and an interval period of  $T/25$ . This section delineates the principal features of coherent modes, encompassing global mode energy and local mode form, through the simultaneous decomposition

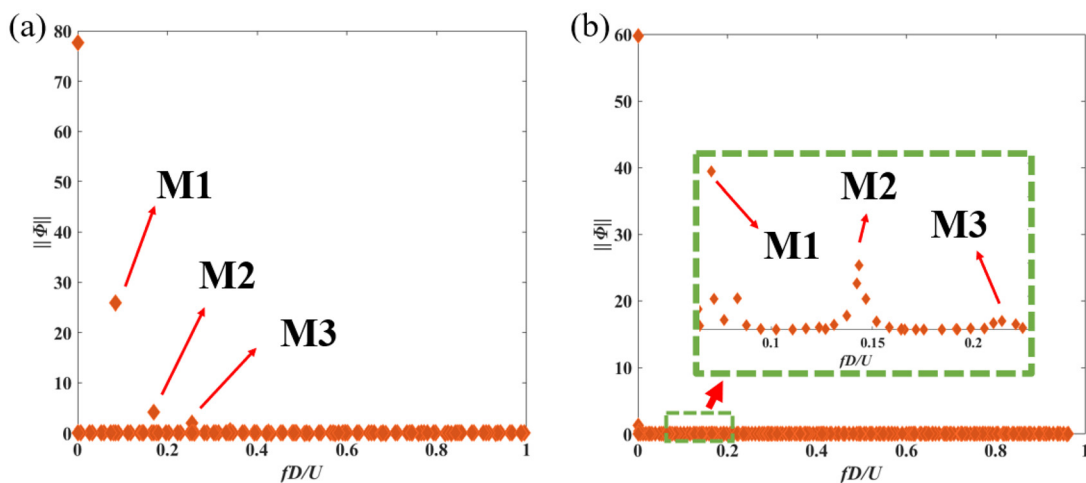


FIG. 11. Mode energy as a function of frequency for (a) baseline case and (b) case 1.

of vorticity fields. As depicted in Fig. 10, the eigenvalues of the principal Ritz mode are predominantly clustered around the unit circle, indicative of a limit cycle oscillation (LCO) state. This clustering phenomenon serves as indirect evidence that this methodology adeptly captures the characteristic frequencies of system dynamics and proficiently approximates the system's vibration modes. In Fig. 11(a), the highest mode energy in each scenario is observed at  $fD/U = 0$ , aligning with the time-averaged mode denoted as M0. Simultaneously, the initial three dynamic modes manifest elevated energy levels in comparison with other modes, as ascertained through their dimensionless frequency, denoted as  $fD/U$  (M1, M2, and M3:  $fD/U = St$ ,  $2St$ , and  $3St$ ). Thus, the wake is consisted by the primary mode (M1) and two superharmonic modes (M2, M3), with the energy of M2 and M3 notably inferior to that of M1. After flow control, the energy of the corresponding order is substantially reduced as shown in Fig. 11(b). The decrease in dynamic mode energy reflects the stability of the flow field. Figure 12 shows the first three orders of vorticity modes for both the baseline case and the jet flow control. Illustrated by Figs. 12(a)–12(c), the vorticity exhibits symmetry for odd orders and antisymmetry for even orders. Since the same color in the vorticity modes represents the same direction of rotation, the anti-symmetric vorticity forms in the even order modes imply that the torque effects cancel each other out. Odd-order modes significantly contribute to the overall activity of the

flow field. Figures 12(d)–12(f) show the first three orders of vorticity modes after jet flow control. Corresponding to Fig. 10(b), it can be found that there is no significant vorticity distribution for the odd-order modes of its contributing action. This indicates that the addition of the jet dramatically reduces the complexity of the flow structure and creates a stable flow field.

For cases 3–5, as depicted in Fig. 8(c)–8(e), a pronounced vortex shedding phenomenon persists. It is evident that the jet only partially suppresses the formation of vortices on the upper side of the model. The vortex distribution on the lower side is affected by the jet to a decreasing extent as the  $Re$  increases. The  $C'_L$  for cases 1–5 and the corresponding baseline cases are shown in Fig. 13. The  $C'_L$  exhibits an upward trend in correspondence with both  $\alpha$  and the  $Re$ . Corresponding to the vortices in Fig. 9, the  $C'_L$  of cases 1 and 2 are reduced by 99.6% and 99.1%, respectively, which achieves a desirable control effect, while cases 3–5 are reduced by 93.1%, 80.2%, and 44.1%, respectively. As depicted in Fig. 7, the flow state on the lower side of the model is not considered, resulting in insufficient control of the flow field. In practical engineering applications, drag reduction typically stands as a primary concern. The drag coefficients are usually large and the average value represents static force acting on the bluff body. The  $(\bar{C}_D)$  mean drag coefficient is decreased, which reflects that the jet contributes to the stabilization.

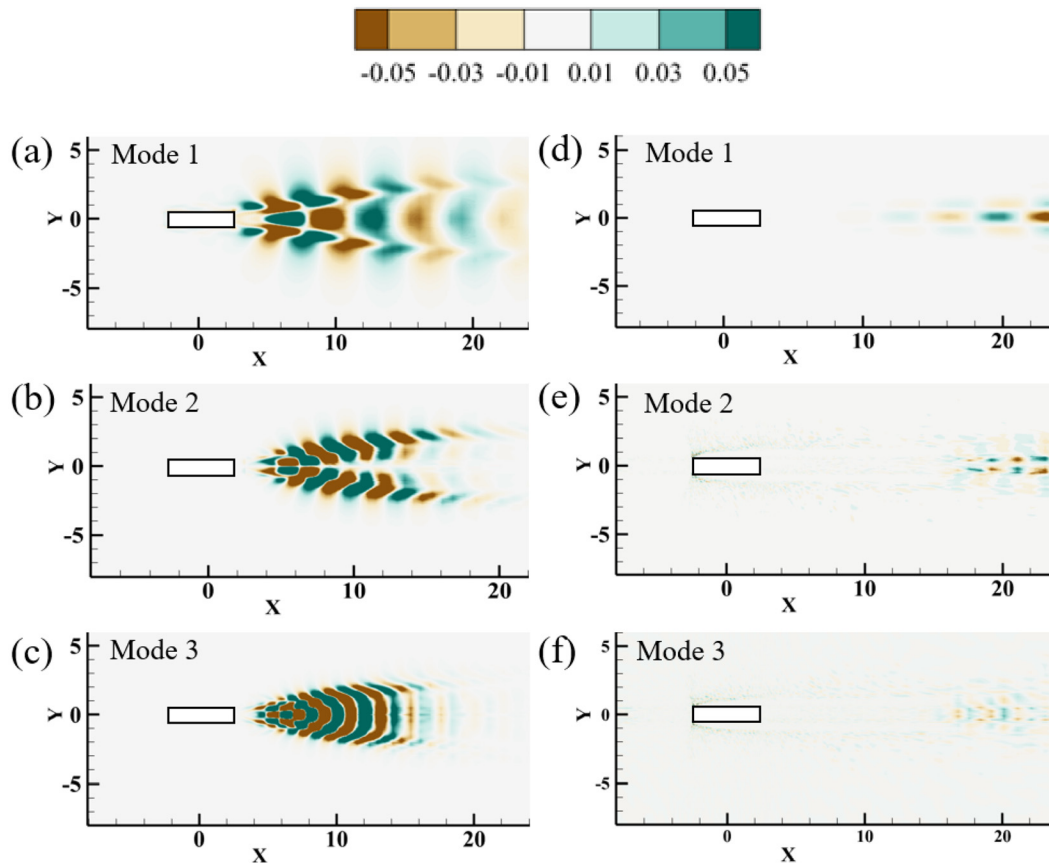


FIG. 12. Vorticity modes for the baseline case and controlled case, where (a)–(c) are the baseline cases and (d)–(f) are the controlled cases.

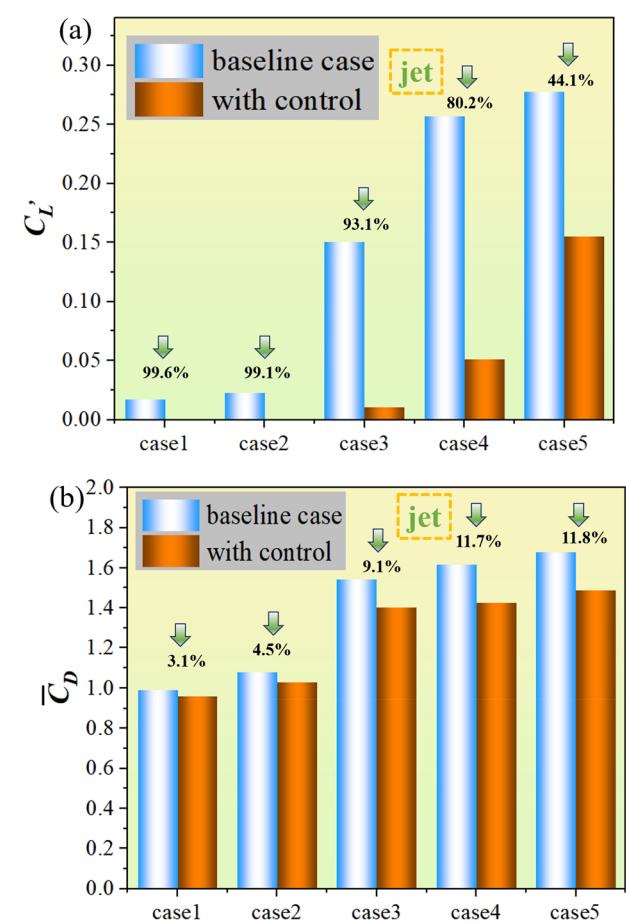


FIG. 13. Comparison of (a)  $C_L'$  (fluctuating lift coefficients) and (b)  $\bar{C}_D$  (mean drag coefficients) for the baseline cases and controlled cases corresponding to cases 1–5.

2. Suction/jet control of airflow orifice B

As depicted in Sec. IV C 1, the effectiveness of cases 3–5 in flow control is suboptimal, attributed to the omission of the influence stemming from the downward sensitive region. This section compares and analyzes the impacts of jet and suction control techniques on the lower flow field of the model. Airflow orifice B is mainly controlled for the lower side flow structure. The implementation of a jet control in airflow orifice B induces an acceleration in the separation of the shear layer on the lower side of the model (Table III). The jet flow control is aimed at accelerating the reattachment process after shear layer separation, crossing the zone where vortex shedding occurs. In contrast, suction control is applied to suppress the separating effect of the shear layer and defer the initiation of vortex shedding.

Figures 13 and 14 show the vortices after jet and suction control. Compared with Figs. 4(c)–4(e), the jet impedes the normal development of the fluid on the lower side, serving as a deceleration mechanism for the separation of the shear layer on the lower side. However, a significant effect of accelerated shear layer attachment has not been achieved. The suction influence, in turn, achieved the intended

TABLE III. Parameters for each case of flow control via airflow orifice B.

Case	Flow angle of attack ( $\alpha$ ) (deg)	Re	Airflow orifice B	
			Flow control	$U_j/U_j$
Case 6	5	150	Jet	1
Case 7		200		
Case 8		250		
Case 9		150	Suction	
Case 10		200		
Case 11		250		

outcome, with a noticeable suppression of shear layer separation. The flow field following suction control resembles the baseline scenario of case 1, suggesting that suction control efficiently alleviates the impact of the flow angle of attack on the flow structure. The comparison shows that the vortex shedding after jet control is more intense than suction control. As shown in Fig. 16, compared with the baseline case, the jet control reduces the  $C_L'$  by 12.4%, 20.6%, and 16.7%; the suction control reduces them by 83.7%, 83.3%, and 78.2%. Meanwhile, the jet

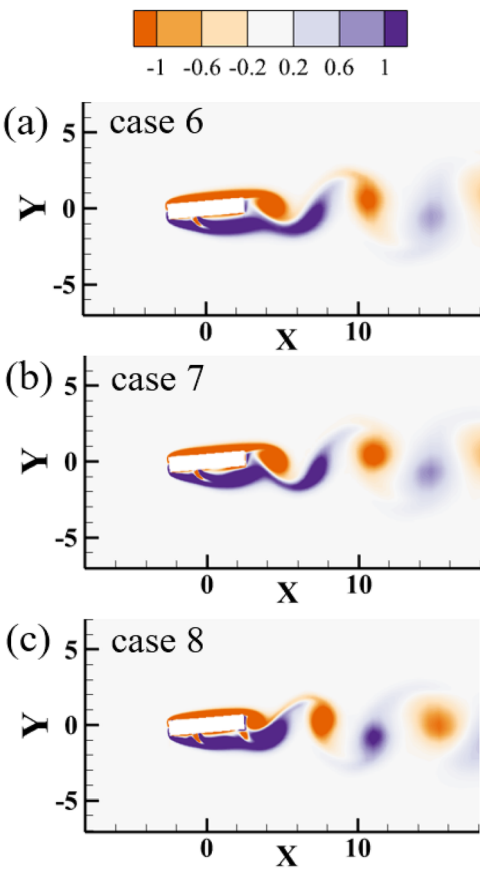


FIG. 14. Vorticity for each case after jet flow control by airflow orifice B: (a) case 6, (b) case 7, and (c) case 8.



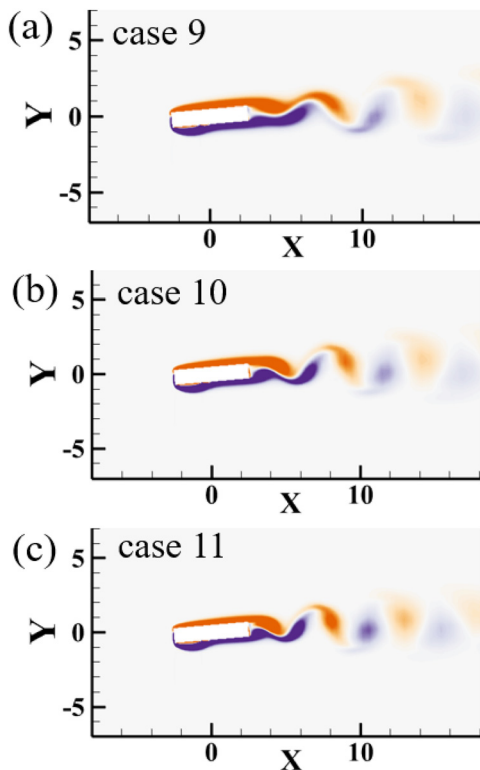


FIG. 15. Vorticity for each case after suction flow control by airflow orifice B: (a) case 9, (b) case 10, and (c) case 11.

control reduces the  $\bar{C}_D$  by 1.1%, 0.7%, and 2.1%; the suction control reduces them by 9.9%, 13.5%, and 15.8%. This indicates that suction control is superior to jet control at the same flow rate. The same applies to the mean drag coefficient. However, the controlled fluctuation values are still not completely suppressed, and the higher the  $Re$ , the less significant the suppression effect. The results show that flow control for high angle of attack cases only through airflow orifice B is not sufficient.

### 3. BVC and the effects of jet flow velocity

In Secs. IV C 1 and IV C 2, it becomes evident that the control of individual air orifices alone is inadequate to attain the desired outcomes at high angle of attack. This section combines airflow orifice A and B to form breath-valve control (BVC), utilizing airflow orifice A for jet flow control and airflow orifice B for more potent suction flow control. The control results are shown in Fig. 17, similar to Figs. 8(a) and 8(b). The issue of excessive separation of the shear layer on the lower side is addressed through suction control at airflow orifice B when solely managed by the jet flow from airflow orifice A. Conversely, when controlled exclusively by suction at airflow orifice B, the vortex shedding phenomenon is mitigated by the jet flow from airflow orifice A. In Figs. 19(a) and 19(b), it can be seen that the  $C'_L$  are reduced by 99.8% and 99.5%, respectively. It is also compared with existing studies, such as Chen *et al.*<sup>30</sup> The results of the wind-tunnel experiments on the bridge model show that the magnitude of the reduction in  $\bar{C}_D$  is in the range of 5%.

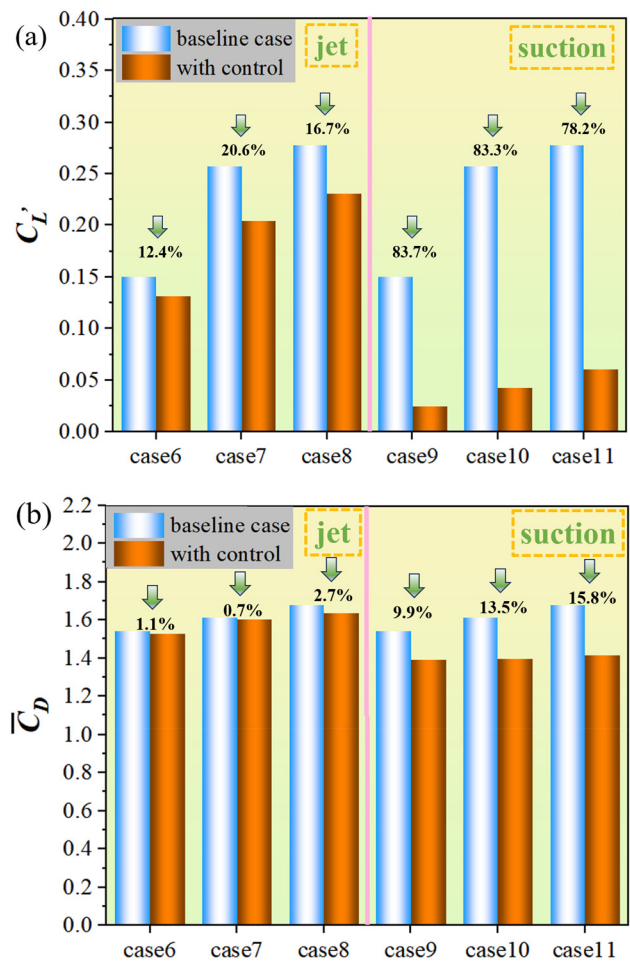


FIG. 16. Comparison of (a)  $C'_L$  (fluctuating lift coefficients) and (b)  $\bar{C}_D$  (mean drag coefficients) for the baseline cases and controlled cases corresponding to cases 6–11.

By our BVC method, the reduction amplitude of  $\bar{C}_D$  can be stabilized at 10% or even higher, and the  $C'_L$  is almost reduced to 0. This fully confirms the rationality and efficiency of combined flow control. The same BVC settings are also applied to the low attack (cases 17 and 18), and it is found that the results are still significant.

However, when  $\alpha$  is set at  $5^\circ$  and  $Re$  is 250, discernible vortices persist at the trailing edge. As depicted in Fig. 18(a), insufficient energy in the jet flow hinders its effective interference with the generation of vortex shedding. Therefore, the kinetic energy input is enhanced by increasing the jet flow velocity. All the combined control cases are shown in Table IV.

When  $Uj = 2$ , there is a dense vortex shedding at the wake, after which the wake becomes smooth. This indicates that the increase in jet flow energy disrupts the original flow structure. The disorganized flow structure accelerates the vortex shedding process and allows the transfer of vortex structure energy into the flow field. The wake flow field quickly enters a state of no vortex shedding. When  $Uj = 3$ , the jet has

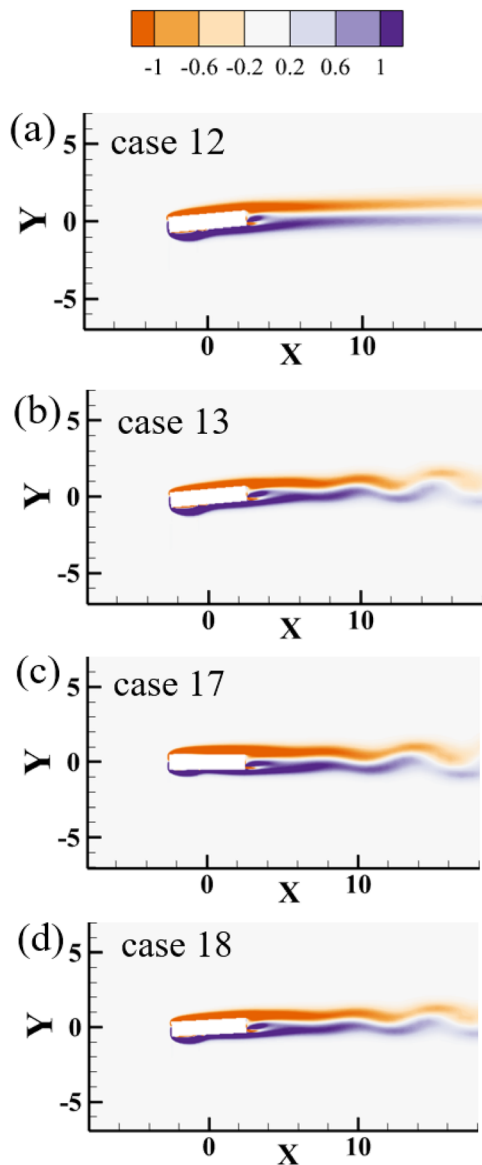


FIG. 17. Vorticity for each case after BVC: (a) case 12, (b) case 13, (c) case 17, and (d) case 18.

taken the dominant position in controlling the wake flow field. At this point, the jet has completely suppressed the vortex shedding of the baseline case, and only the weak vortex shedding phenomenon generated by the self-generation of the jet occurs. Corresponding to Figs. 18(d)–18(f), the velocity gradient of the mean flow velocity in the  $X$  direction also increases rapidly with the increase in  $U_j$ , and the region of variation gradually narrows. Flow rates exhibiting rapid variation within a limited range signify the high efficiency of flow control. As shown in Fig. 19, the  $C_L'$  are reduced by 95.5%, 96.1%, and 99.7%, respectively. An elevated jet velocity has a marginal impact on the control of  $C_D$  while exerting no discernible influence on the overall

control. Therefore, increasing the wake flow velocity can effectively stifle the potential flow-induced vibration.

To intuitively observe the variation in vortex shedding,  $PSD$  for controlled cases is acquired and compared with those under different flow rates. The vortex shedding frequency can directly reflect the control effect. As shown in Fig. 20(a), the relevant cases are taken with  $\alpha = 5^\circ$ ,  $Re = 150$ : baseline case, case 3, case 6, case 9, and case 12. The primary vortex shedding frequencies corresponding to the above cases are 0.1162, 0.0694, 0.0677, and 0.0851, respectively (case 12 has no obvious vortex shedding phenomenon). Case 3 effectively retards the initiation of vortex shedding in the wake, resulting in a reduction in both frequency and peak value. In contrast, case 6 introduces a substantial amount of kinetic energy into the lower shear layer, leading to a decrease in frequency and an increase in peak value. Case 9 delayed the separation of the lower shear layer due to the suction control of air-flow orifice B, but still produced a vortex shedding at the wake similar to the no-angle of attack case. Thus the vortex shedding frequency of case 9 is closer to the baseline case. Figure 20(b) reflects the vortex shedding for various flow velocity controls, and the primary vortex shedding frequencies corresponding to the four cases are 0.1142, 0.1008, 0.2165, and 0.3428, respectively. Case 14 exhibited negligible alteration in the flow state, exerting only a subtle influence, consequently leading to a slight reduction in the frequency of vortex shedding. In contrast, cases 15 and 16 change the wake flow structure due to the increased jet flow energy. The dense vortex shedding phenomenon illustrated in Fig. 18 corresponds to an increased vortex shedding frequency, as well as a reduced peak value.

## V. CONCLUSIONS

In this study, two-dimensional numerical simulations are first carried out in a rectangular cylinder ( $AR = 5$ ) with flow angle of attack ( $\alpha$ ) in the range of  $0^\circ$ – $5^\circ$  and the Reynolds number ( $Re$ ) in the range of 100–300. Five representative cases are selected from the simulation results. Global linear instability, adjoint mode, and sensitivity analysis are performed to identify the optimal location for introducing the jet/suction flow. Then, higher-order dynamic mode deception (HODMD), lift coefficient fluctuation ( $C_L'$ ) value comparison, and power spectral discipline ( $PSD$ ) are employed to validate the rationality and effectiveness of the active flow control.

- (1) The elevation of both flow angle of attack and  $Re$  results in an augmentation of  $C_{L-RMS}$  for rectangular cylinders ( $AR = 5$ ), with the impact of  $\alpha$  being more pronounced. The  $PSD$  peak value corresponding to the primary vortex shedding frequency for each case shows that higher  $Re$  corresponds to higher energy at high  $\alpha$ . The instantaneous vorticity further demonstrates that the escalation of both  $\alpha$  and  $Re$  gives rise to more pronounced vortex shedding phenomena. The increase in  $\alpha$  accelerates the separation of the shear layer in the spatial structure, which is exacerbated by the increase in the  $Re$ .
- (2) The leading direct/adjoint global modes ( $\alpha = 0^\circ$ ,  $Re = 200$ ;  $\alpha = 2^\circ$ ,  $Re = 200$ ;  $\alpha = 5^\circ$ ,  $Re = 150$ ;  $\alpha = 5^\circ$ ,  $Re = 200$ ; and  $\alpha = 5^\circ$ ,  $Re = 250$ ) are extracted for representative cases. The mode characteristics progressively transition from a symmetric configuration to a downwind-inclined form with the augmentation of  $\alpha$  and  $Re$ . Concurrently, the direct modes reveal a more intricate and well-defined mode distribution beneath the model, while the adjoint modes display a clustering of mode distribution

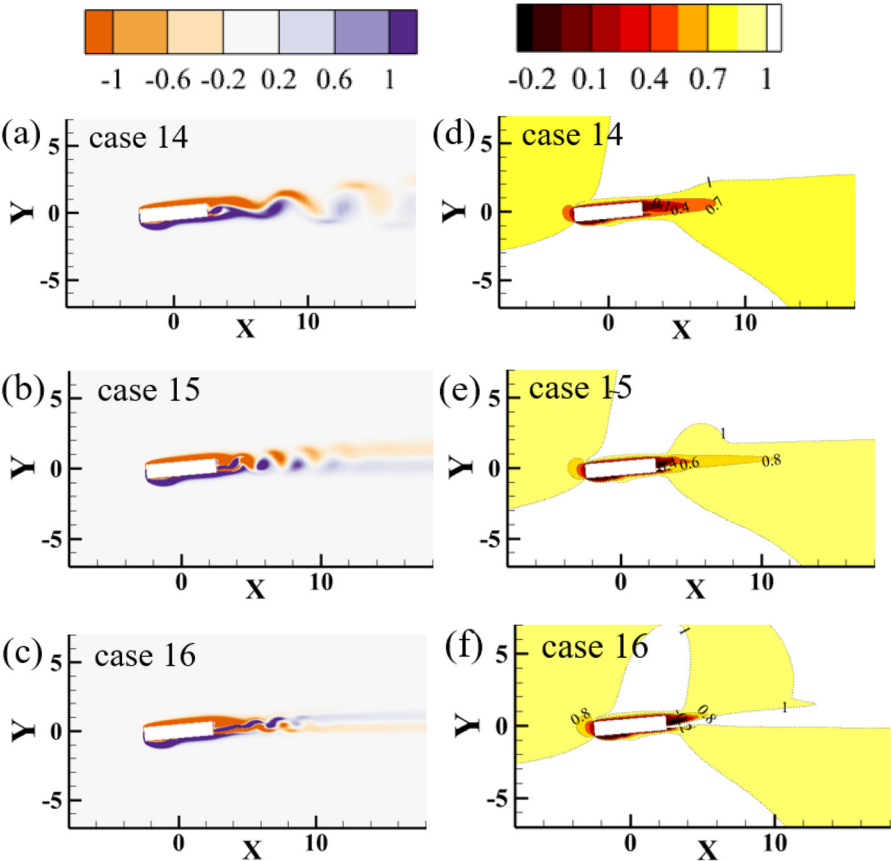


FIG. 18. Vorticity and mean flow velocity in x direction for cases 14–16, where (a)–(c) are the vorticity and (d)–(f) are the x-direction mean flow velocity.

toward the leeward and downwind sides of the model. The sensitivity map visualizes that when  $\alpha=0^\circ$ , the sensitive region exists only at the leeward side. As  $\alpha$  is raised to  $5^\circ$ , the sensitive region gradually shifts from the leeward to the downwind side. The increase in the  $Re$  makes the sensitive region on the down-side wider and more pronounced. Therefore, the region of flow control is determined on the leeward and downwind side of the model.

- (3) The leeward side is always a sensitive region, so flow control at the leeward side is considered separately first. A jet is

TABLE IV. Parameters for each case of BVC.

Case	Flow angle of attack (deg)	Re	Orifice A		Orifice B	
			Flow control	$U_j$	Flow control	$U_s$
Case 12	5	150	Jet	1	Suction	1
Case 13		200		1		
Case 14		250		1		
Case 15		250		2		
Case 16		250		3		
Case 17	0	200		1		
Case 18	2	200		1		

employed to impede the separation of the shear layer, and air-flow orifice A is configured with a jet velocity ( $U_j$ ) of 1. The results show that case 1 and case 2 are highly effective in suppressing the vortex shedding phenomenon, and the  $C'_L$  are reduced by 99.6% and 99.1%, respectively. Meanwhile, higher-order dynamic mode decomposition (HODMD) is employed to elaborate the mechanism of case 1 and its corresponding baseline case. Odd-order modes, exhibiting symmetric forms in the vorticity, contribute significantly to the overall activity of the flow field. The odd-order modes exhibit no notable vortex shedding distribution following jet control, and the energy of each order is effectively suppressed to a very low state. Therefore, the jet control on the leeward side at low  $\alpha$  is significant.

- (4) Cases 3–5 experience reductions of only 93.1%, 80.2%, and 44.1%, respectively, as flow control in the sensitive region on the lower side is not considered. Active flow control is performed at airflow orifice B using jet and suction, respectively (cases 6–11). The jet flow control aims to accelerate the separation of the shear layer and advance the reattachment process. The suction is to avoid accelerated shear layer separation due to the spatial structure caused by the  $\alpha$ . The results show that the jet control reduces the  $C'_L$  by 12.4%, 20.6%, and 16.7%, while the suction control reduces it by 83.7%, 83.3%, and 78.2%. Suction flow control is far superior to jet flow control.

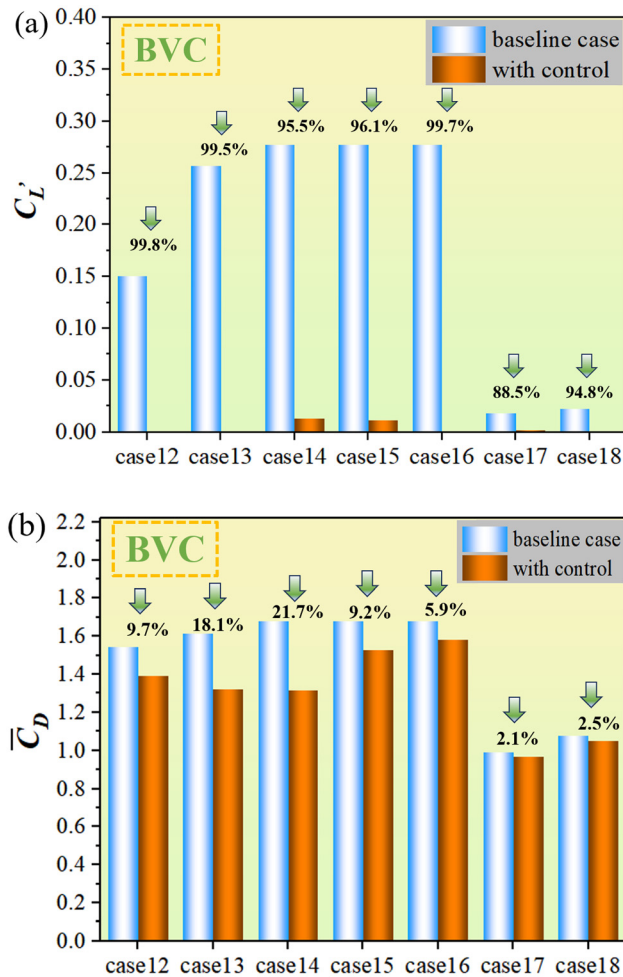


FIG. 19. Comparison of (a)  $C_L'$  (fluctuating lift coefficients) and (b)  $C_D$  (mean drag coefficients) corresponding to cases 12–18.

(5) Breath-valve control (BVC) method is proposed to achieve more desirable results (cases 12–18). BVC aims to achieve a process of flow recirculation without adding additional mass sources and exhaust measures. This methodology simplifies the control system design, guaranteeing the comprehensive utilization of flow within the system for flow control, thereby enhancing energy efficiency. The  $C_L'$  of case 12 and case 13 reduces by 99.8% and 99.5%, and  $C_D$  of them reduces by 9.7% and 18.1%. The substantial decrease in drag also indicates a reduction in the flow disturbance experienced by the model. At  $\alpha = 5^\circ$  and  $Re = 250$ , the control effect is enhanced through the augmentation of flow velocity on the leeward side. The mean flow velocity in the X direction elucidates the predominant influence of the high-velocity jet in disrupting the formation of wake vortices.  $C_L'$  decreases by 95.5%, 96.1%, and 99.7% for cases 14–16 setting various jet flow velocities. The change in jet velocity mitigates the instability caused by the elevated  $Re$ . Concurrently, implementing suction control on the lower side of the model when

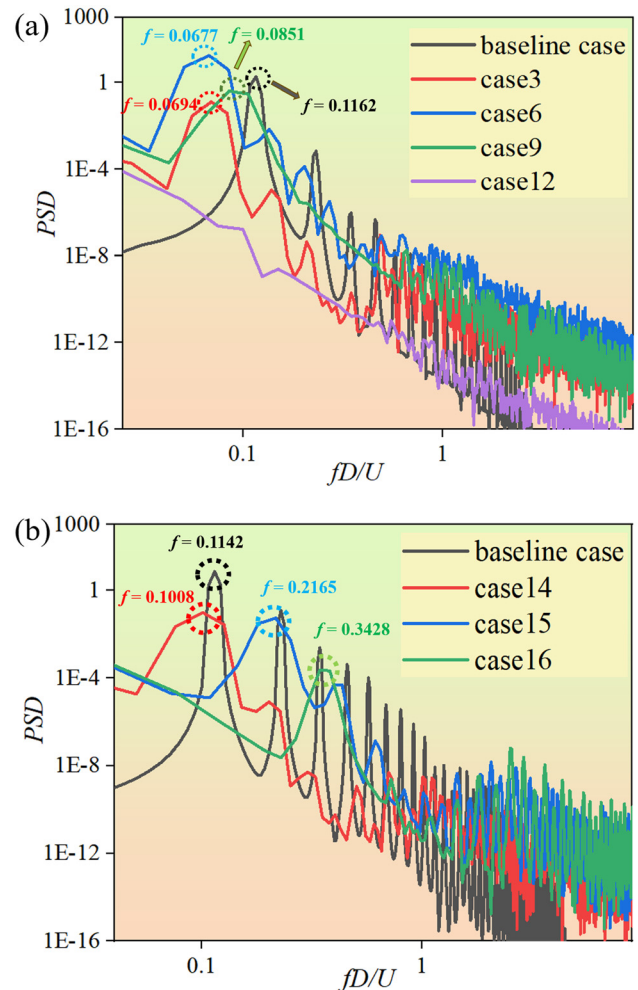


FIG. 20. PSD for (a) each control method and (b) various jet flow velocities.

fluid flows in the positive  $\alpha$  direction effectively mitigates the issue of excessively rapid shear layer separation induced by  $\alpha$ . To explore the universality of BVC, cases 1 and 2 are also controlled with BVC (cases 17 and 18). Individual leeward jet control is only slightly better than the BVC, suggesting that the BVC still performs well at low angle of attack. The BVC effectively achieves the outcomes initiated by traditional suction or jet flow across all angle of attack. Optimal control can be accomplished by adjusting the flow rate.

This paper describes the prediction of flow control regions by linear stability and sensitivity analysis. Two active control methods, jet and suction, and BVC are also compared. This study aims to provide meaningful insights into flow control strategies for common mechanical component forms to reduce the potential risk of flow-induced vibrations.

## ACKNOWLEDGMENTS

This work is supported by the National Natural Science Foundation of China (Grant No. 12172109 and 51908107), by the



Guangdong Basic and Applied Basic Research Foundation under grant 2022A1515011492, and by the Shenzhen Science and Technology Program under grant JCYJ20220531095605012.

## AUTHOR DECLARATIONS

### Conflict of Interest

The authors have no conflicts to disclose.

## Author Contributions

**Qingchi Zhu:** Data curation (equal); Investigation (equal); Methodology (equal); Resources (equal); Software (equal); Visualization (equal); Writing – original draft (equal). **Lei Zhou:** Conceptualization (equal); Formal analysis (equal); Methodology (equal); Validation (equal); Writing – review & editing (equal). **Hongfu Zhang:** Conceptualization (equal); Funding acquisition (equal); Project administration (equal); Resources (equal); Software (equal); Writing – review & editing (equal). **Kam Tim Tse:** Conceptualization (equal); Formal analysis (equal); Methodology (equal); Writing – review & editing (equal). **Hui Tang:** Conceptualization (equal); Formal analysis (equal); Methodology (equal); Writing – review & editing (equal). **Bernd R. Noack:** Conceptualization (equal); Formal analysis (equal); Methodology (equal); Project administration (equal); Writing – review & editing (equal).

## DATA AVAILABILITY

The data that support the findings of this study are available from the corresponding author upon reasonable request.

## REFERENCES

- <sup>1</sup>F. Xu, H. Yu, M. Zhang, and Y. Han, “Experimental study on aerodynamic characteristics of a large-diameter ice-accreted cylinder without icicles,” *J. Wind Eng. Ind. Aerodyn.* **208**, 104453 (2021).
- <sup>2</sup>M. Matsumoto, T. Yagi, Y. Shigemura, and D. Tsushima, “Vortex-induced cable vibration of cable-stayed bridges at high reduced wind velocity,” *J. Wind Eng. Ind. Aerodyn.* **89**, 633 (2001).
- <sup>3</sup>G.-B. Chen and W.-L. Chen, “Characteristics of aerodynamic force and flow structure behind single box girder under isolated slit control,” *J. Central South Univ.* **29**(8), 2542–2557 (2022).
- <sup>4</sup>X.-F. Tian, *et al.*, “Dynamic response analysis of high-speed maglev train-guideway system under crosswinds,” *J. Central South Univ.* **30**(8), 2757–2771 (2023).
- <sup>5</sup>M. M. Alam, T. Abdelhamid, and A. Sohankar, “Effect of cylinder corner radius and angle of attack on heat transfer and flow topology,” *Int. J. Mech. Sci.* **175**, 105566 (2020).
- <sup>6</sup>L. Zhou, K. T. Tse, G. Hu, and Y. Li, “Higher order dynamic mode decomposition of wind pressures on square buildings,” *J. Wind Eng. Ind. Aerodyn.* **211**, 104545 (2021).
- <sup>7</sup>F. Deng, M. Zhao, S. Qin, *et al.*, “Numerical simulation study on the dynamics of bluff-body flames under oxygen-lean conditions,” *Energies* **17**(1), 142 (2023).
- <sup>8</sup>H. Zhang, L. Zhou, and T. K. T. Tse, “Mode-based energy transfer analysis of flow-induced vibration of two rigidly coupled tandem cylinders,” *Int. J. Mech. Sci.* **228**, 107468 (2022).
- <sup>9</sup>C. Hu, L. Zhao, and Y. Ge, “Wind-induced instability mechanism of old tacoma narrows bridge from aerodynamic work perspective,” *J. Bridge Eng.* **27**, 04022029 (2022).
- <sup>10</sup>D. Gao, Z. Deng, W. Yang, and W. Chen, “Review of the excitation mechanism and aerodynamic flow control of vortex-induced vibration of the main girder for long-span bridges: A vortex-dynamics approach,” *J. Fluids Struct.* **105**, 103348 (2021).
- <sup>11</sup>H. Choi, W.-P. Jeon, and J. Kim, “Control of flow over a bluff body,” *Annu. Rev. Fluid Mech.* **40**, 113 (2008).
- <sup>12</sup>T. R. Sahu, M. Furquan, Y. Jaiswal, and S. Mittal, “Flow-induced vibration of a circular cylinder with rigid splitter plate,” *J. Fluids Struct.* **89**, 244 (2019).
- <sup>13</sup>L. Lu, M.-m. Liu, B. Teng, Z.-d. Cui, G.-q. Tang, M. Zhao, and L. Cheng, “Numerical investigation of fluid flow past circular cylinder with multiple control rods at low Reynolds number,” *J. Fluids Struct.* **48**, 235 (2014).
- <sup>14</sup>S. Huang, “VIV suppression of a two-degree-of-freedom circular cylinder and drag reduction of a fixed circular cylinder by the use of helical grooves,” *J. Fluids Struct.* **27**, 1124 (2011).
- <sup>15</sup>S. Scott Collis, R. D. Joslin, A. Seifert, and V. Theofilis, “Issues in active flow control: Theory, control, simulation, and experiment,” *Prog. Aerosp. Sci.* **40**, 237 (2004).
- <sup>16</sup>M. Jahanmiri, “Active flow control: A review,” Report No. 12 (2010).
- <sup>17</sup>C.-Y. Ma, H.-Y. Xu, and C.-L. Qiao, “Comparative study of two combined blowing and suction flow control methods on pitching airfoils,” *Phys. Fluids* **35**, 035120 (2023).
- <sup>18</sup>Y. Delaunay and L. Kaiktsis, “Control of circular cylinder wakes using base mass transpiration,” *Phys. Fluids* **13**, 3285 (2001).
- <sup>19</sup>J. H. M. Franssón, P. Konieczny, and P. H. Alfredsson, “Flow around a porous cylinder subject to continuous suction or blowing,” *J. Fluids Struct.* **19**, 1031 (2004).
- <sup>20</sup>W.-L. Chen, D.-B. Xin, F. Xu, H. Li, J.-P. Ou, and H. Hu, “Suppression of vortex-induced vibration of a circular cylinder using suction-based flow control,” *J. Fluids Struct.* **42**, 25 (2013).
- <sup>21</sup>D. Gao, G. Chen, W. Chen, Y. Huang, and H. Li, “Active control of circular cylinder flow with windward suction and leeward blowing,” *Exp. Fluids* **60**, 26 (2019).
- <sup>22</sup>Z. Wang, D. Fan, X. Jiang, M. S. Triantafyllou, and G. E. Karniadakis, “Deep reinforcement transfer learning of active control for bluff body flows at high Reynolds number,” *J. Fluid Mech.* **973**, A32 (2023).
- <sup>23</sup>K. Lam, Y. F. Lin, L. Zou, and Y. Liu, “Numerical study of flow patterns and force characteristics for square and rectangular cylinders with wavy surfaces,” *J. Fluids Struct.* **28**, 359 (2012).
- <sup>24</sup>X. Sun, C. Steve Suh, C. Sun, and B. Yu, “Vortex-induced vibration of a flexible splitter plate attached to a square cylinder in laminar flow,” *J. Fluids Struct.* **101**, 103206 (2021).
- <sup>25</sup>H. Meng, W. Chen, G. Chen, D. Gao, and H. Li, “Characteristics of forced flow past a square cylinder with steady suction at leading-edge corners,” *Phys. Fluids* **34**, 025119 (2022).
- <sup>26</sup>A. Ahmed, R. Manzoor, S. U. Islam, and H. Rahman, “Numerical investigation for flow over a square rod through a passive control method at various Reynolds numbers,” *Can. J. Phys.* **98**, 425 (2019).
- <sup>27</sup>D. Gao, H. Meng, Y. Huang, G. Chen, and W.-L. Chen, “Active flow control of the dynamic wake behind a square cylinder using combined jets at the front and rear stagnation points,” *Phys. Fluids* **33**, 047101 (2021).
- <sup>28</sup>Y. Ran, W.-L. Chen, Y. Cao, H. Li, and D. Gao, “On the distributed blowing control of flow around a square cylinder at a low Reynolds number,” *Ocean Eng.* **285**, 115240 (2023).
- <sup>29</sup>H. Zhang, D. Xin, and J. Ou, “Wake control of vortex shedding based on spanwise suction of a bridge section model using delayed detached eddy simulation,” *J. Wind Eng. Ind. Aerodyn.* **155**, 100 (2016).
- <sup>30</sup>G.-B. Chen, W.-L. Chen, D.-L. Gao, and Z.-F. Yang, “Active control of flow structure and unsteady aerodynamic force of box girder with leading-edge suction and trailing-edge jet,” *Exp. Therm. Fluid Sci.* **120**, 110244 (2021).
- <sup>31</sup>D. Bäder, T. Indinger, N. A. Adams, P. Unterlechner, and G. Wickern, “Interference effects of cooling airflows on a generic car body,” *J. Wind Eng. Ind. Aerodyn.* **119**, 146 (2013).
- <sup>32</sup>A. Purohit, A. K. Darpe, and S. P. Singh, “Influence of flow velocity and flexural rigidity on the flow induced vibration and acoustic characteristics of a flexible plate,” *J. Vib. Control* **24**, 2284 (2017).
- <sup>33</sup>S. C. Yen and L.-C. Huang, “Reynolds number effects on flow characteristics and aerodynamic performances of a swept-back wing,” *Aerosp. Sci. Technol.* **15**, 155 (2011).
- <sup>34</sup>Z. N. Gianikos, B. A. Kirschmeier, A. Gopalaramnam, and M. Bryant, “Limit cycle characterization of an aeroelastic wing in a bluff body wake,” *J. Fluids Struct.* **95**, 102986 (2020).

- <sup>35</sup>Z. Song, M. Duan, and J. Gu, "Numerical investigation on the suppression of VIV for a circular cylinder by three small control rods," *Appl. Ocean Res.* **64**, 169 (2017).
- <sup>36</sup>T. T. Ma, L. Zhao, S. Y. Cao, Y. J. Ge, and H. Miyagi, "Investigations of aerodynamic effects on streamlined box girder using two-dimensional actively-controlled oncoming flow," *J. Wind Eng. Ind. Aerodyn.* **122**, 118 (2013).
- <sup>37</sup>Y. Ito, H. Shirato, and M. Matsumoto, "Coherence characteristics of fluctuating lift forces for rectangular shape with various fairing decks," *J. Wind Eng. Ind. Aerodyn.* **135**, 34 (2014).
- <sup>38</sup>See <http://www.aniv-iawe.org/barc> for G. Bartoli, L. Bruno, G. Buresti, F. Ricciardelli, M. V. Salvetti, and A. Zasso, "BARC overview document," 2008; accessed 27 August 2011.
- <sup>39</sup>D. T. Nguyen, D. M. Hargreaves, and J. S. Owen, "Vortex-induced vibration of a 5:1 rectangular cylinder: A comparison of wind tunnel sectional model tests and computational simulations," *J. Wind Eng. Ind. Aerodyn.* **175**, 1 (2018).
- <sup>40</sup>G. Zhu, S. Huang, and Q. S. Li, "Large-eddy simulation of the inflow turbulence transport and aerodynamics of a rectangular 5:1 cylinder with high-order numerical methods," *J. Wind Eng. Ind. Aerodyn.* **207**, 104366 (2020).
- <sup>41</sup>R. Ma, Q. Zhou, P. Wang, Y. Yang, M. Li, and S. Cao, "Effects of sinusoidal streamwise gust on the vortex-induced force on an oscillating 5:1 rectangular cylinder," *J. Wind Eng. Ind. Aerodyn.* **213**, 104642 (2021).
- <sup>42</sup>L. Bruno, M. V. Salvetti, and F. Ricciardelli, "Benchmark on the Aerodynamics of a Rectangular 5:1 Cylinder: An overview after the first four years of activity," *J. Wind Eng. Ind. Aerodyn.* **126**, 87 (2014).
- <sup>43</sup>T.-H. Le, M. Matsumoto, and H. Shirato, "Spanwise coherent structure of wind turbulence and induced pressure on rectangular cylinders," *Wind Struct.* **12**, 441 (2009).
- <sup>44</sup>G. Schewe, "Reynolds-number-effects in flow around a rectangular cylinder with aspect ratio 1:5," *J. Fluids Struct.* **39**, 15 (2013).
- <sup>45</sup>J. F. Derakhshandeh and M. M. Alam, "A review of bluff body wakes," *Ocean Eng.* **182**, 475 (2019).
- <sup>46</sup>Y. Bao, C. Huang, D. Zhou, J. Tu, and Z. Han, "Two-degree-of-freedom flow-induced vibrations on isolated and tandem cylinders with varying natural frequency ratios," *J. Fluids Struct.* **35**, 50 (2012).
- <sup>47</sup>R. Bhatt and M. M. Alam, "Vibrations of a square cylinder submerged in a wake," *J. Fluid Mech.* **853**, 301 (2018).
- <sup>48</sup>Z. Han, D. Zhou, A. Malla, R. Nepali, V. Kushwaha, Z. Li, K. C. S. Kwok, J. Tu, and Y. Bao, "Wake-induced vibration interference between a fixed square cylinder and a 2-DOF downstream square cylinder at low Reynolds numbers," *Ocean Eng.* **164**, 698 (2018).
- <sup>49</sup>R. Nepali, H. Ping, Z. Han, D. Zhou, H. Yang, J. Tu, Y. Zhao, and Y. Bao, "Two-degree-of-freedom vortex-induced vibrations of two square cylinders in tandem arrangement at low Reynolds numbers," *J. Fluids Struct.* **97**, 102991 (2020).
- <sup>50</sup>Q. Zhu, L. Zhou, J. Wen, T. Liu, J. Zhang, H. Tang, and H. Zhang, "Laminar flow over a rectangular cylinder experiencing torsional flutter: Dynamic response, forces and coherence modes," *Phys. Fluids* **35**, 093610 (2023).
- <sup>51</sup>T. Abdelhamid, A. G. Rahma, M. M. Alam, R. Chen, M. Islam, Q. Zhou, and H. Zhu, "Heat transfer and flow around curved corner cylinder: Effect of attack angle," *SN Appl. Sci.* **5**, 163 (2023).
- <sup>52</sup>T. Sun, C. Shi, G. Zhang, Z. Zong, and H. Wang, "Experimental study on the influence of the angle of attack on cavity evolution and surface load in the water entry of a cylinder," *Ocean Eng.* **219**, 108271 (2021).
- <sup>53</sup>D. Tang and E. H. Dowell, "Experimental aerodynamic response for an oscillating airfoil in buffeting flow," *AIAA J.* **52**, 1170 (2014).
- <sup>54</sup>W. L. Keith, K. M. Cipolla, D. R. Hart, and D. A. Furey, "Drag measurements on long thin cylinders at small angles and high Reynolds numbers," *Exp. Fluids* **38**, 759 (2005).
- <sup>55</sup>E. Boujo, "Second-order adjoint-based sensitivity for hydrodynamic stability and control," *J. Fluid Mech.* **920**, A12 (2021).
- <sup>56</sup>J. Li and M. Zhang, "Reinforcement-learning-based control of confined cylinder wakes with stability analyses," *J. Fluid Mech.* **932**, A44 (2022).
- <sup>57</sup>F. Giannetti and P. Luchini, "Structural sensitivity of the first instability of the cylinder wake," *J. Fluid Mech.* **581**, 167 (2007).
- <sup>58</sup>P. Meliga, G. Pujals, and É. Serre, "Sensitivity of 2-D turbulent flow past a D-shaped cylinder using global stability," *Phys. Fluids* **24**, 061701 (2012).
- <sup>59</sup>Y. Wang, E. Ferrer, J. Saavedra, G. Paniagua, and E. Valero, "Stability-analysis-based optimization to control flow separation over a diffusing passage," *Phys. Fluids* **33**, 014103 (2021).
- <sup>60</sup>L. Zhou, H. Li, T. K. T. Tse, X. He, G. Y. C. Maceda, and H. Zhang, "Sensitivity-aided active control of flow past twin cylinders," *Int. J. Mech. Sci.* **242**, 108013 (2023).
- <sup>61</sup>S. Le Clainche and J. M. Vega, "Higher order dynamic mode decomposition," *SIAM J. Appl. Dyn. Syst.* **16**, 882 (2017).
- <sup>62</sup>N. Benito, J. R. Arias, A. Velazquez, and J. M. Vega, "Real time performance improvement of engineering control units via higher order singular value decomposition: Application to a SI engine," *Control Eng. Pract.* **19**, 1315 (2011).
- <sup>63</sup>S. Le Clainche and J. M. Vega, "Higher order dynamic mode decomposition to identify and extrapolate flow patterns," *Phys. Fluids* **29**, 084102 (2017).
- <sup>64</sup>H. Zhang, L. Zhou, T. Liu, Z. Guo, and F. Golnary, "Dynamic mode decomposition analysis of the two-dimensional flow past two transversely in-phase oscillating cylinders in a tandem arrangement," *Phys. Fluids* **34**, 033602 (2022).
- <sup>65</sup>S. Le Clainche, J. M. Vega, and J. Soria, "Higher order dynamic mode decomposition of noisy experimental data: The flow structure of a zero-net-mass-flux jet," *Exp. Therm. Fluid Sci.* **88**, 336 (2017).
- <sup>66</sup>Z. Liu, *et al.*, "Primary instability, sensitivity and active control of flow past two tandem circular cylinders," *Ocean Eng.* **294**, 116863 (2024).
- <sup>67</sup>C. Chen and D. Wang, "Active flow control of a high-speed train wake using synthetic jets," *Flow. Turbul. Combust.* **111**, 439 (2023).
- <sup>68</sup>H. Yu, W.-L. Chen, Z. Xu, H. Li, and D. Gao, "Wake stabilization behind a cylinder by secondary flow over the leeward surface," *Phys. Fluids* **34**, 055110 (2022).
- <sup>69</sup>W.-L. Chen, Y. Huang, C. Chen, H. Yu, and D. Gao, "Review of active control of circular cylinder flow," *Ocean Eng.* **258**, 111840 (2022).
- <sup>70</sup>C. Geuzaine and J.-F. Remacle, "Gmsh: A 3-D finite element mesh generator with built-in pre- and post-processing facilities," *Numer. Meth. Eng.* **79**, 1309 (2009).
- <sup>71</sup>K. Hourigan, M. C. Thompson, and B. T. Tan, "Self-sustained oscillations in flows around long blunt plates," *J. Fluids Struct.* **15**, 387 (2001).
- <sup>72</sup>Y. Nakamura and T. Yoshimura, "Flutter and vortex excitation of rectangular prisms in pure torsion in smooth and turbulent flows," *J. Sound Vib.* **84**, 305 (1982).